Lappeenranta
University of Technology

Heikki Pitkänen

FIRST PRINCIPLES MODELING OF METALLIC ALLOYS AND ALLOY SURFACES

Thesis for the degree of Doctor of Science (Technology) to be presented with due permission for public examination and criticism in the Auditorium 1383 at Lappeenranta University of Technology, Lappeenranta, Finland on the 29th of October, 2010, at noon.

Acta Universitatis
Lappeenrantaensis 401

Supervisor Professor Matti Alatalo
Department of Mathematics and Physics
Lappeenranta University of Technology
Lappeenranta, Finland

Reviewers Professor Tapio Rantala
Department of Physics
Tampere University of Technology
Tampere, Finland

Professor Kai Nordlund
Department of Physics
Helsinki Institute of Physics
Helsinki, Finland

Opponent Professor Srinivasan G. Srivilliputhur
Department of Materials Science and Engineering
University of North Texas
Denton, Texas, USA

ISBN 978-952-214-983-1
ISBN 978-952-214-984-8 (PDF)
ISSN 1456-4491

Lappeenrannan teknillinen yliopisto
Digipaino

Abstract

Heikki Pitkänen
First principles modeling of metallic alloys and alloy surfaces
Lappeenranta 2009
53 p.
Acta Universitatis Lappeenrantaensis 401
Diss. Lappeenranta University of Technology
ISBN 978-952-214-983-1, ISBN 978-952-214-984-8 (PDF), ISSN 1456-4491

By alloying metals with other materials, one can modify the metal's characteristics, or compose an alloy which has certain desired characteristics that no pure metal has. The field is vast and complex, and phenomena that govern the behaviour of alloys are numerous. Theories cannot penetrate such complexity, and the scope of experiments is also limited. This is why the relatively new field of *ab initio* computational methods has much to give to this field. With these methods, one can extend the understanding given by theories, predict how some systems might behave, and be able to obtain information that is not there to see in physical experiments.

This thesis pursues to contribute to the collective knowledge of this field in the light of two cases. The first part examines the oxidation of Ag/Cu, namely, the adsorption dynamics and oxygen induced segregation of the surface. Our results demonstrate that the presence of Ag on the Cu(100) surface layer strongly inhibits dissociative adsorption. Our results also confirmed that surface reconstruction does happen, as experiments predicted. Our studies indicate that 0.25 ML of oxygen is enough for Ag to diffuse towards the bulk, under the copper oxide layer.

The other part elucidates the complex interplay of various energy and entropy contributions to the phase stability of paramagnetic duplex steel alloys. We were able to produce a phase stability map from first principles, and it agrees with experiments rather well. Our results also show that entropy contributions play a very important role on defining the phase stability. This is, to the author's knowledge, the first *ab initio* study upon this subject.

Keywords: *metal surfaces, oxidation, first principles calculations, duplex steels*
UDC 669 : 539.211 : 542.943

Preface

This thesis was prepared at Lappeenranta University of Technology, partly in the Department of Electrical Engineering, Laboratory of Electronics Materials Science, and partly in the Department of Mathematics and physics, Laboratory of Applied Mathematics, under the guidance of Prof. Matti Alatalo during the years 2004-2010.

I would like to thank my supervisor Matti Alatalo for his invaluable guidance and his encouraging and positive attitude, my important collaborator and advisor Levente Vitos for his help using the EMTO code, and his indispensable involvement in the steel papers. I would also like to thank my colleagues (Antti, Matti, Sami, Katariina, Nelli, Heli and Arto) for creating a positive and motivating atmosphere towards what we do. Special thanks to Antti Puisto for his advice and insight. I would also like to thank Matti Ropo for his help using the EMTO code.

I wish to thank all the people with whom I have had the pleasure and the privilege to collaborate over the years: The people of surface science laboratory of TUT, laboratory of physics in HUT, and laboratory of chemistry at the University of Oulu.

I acknowledge the rewievers Professor Tapio Rantala and Professor Kai Nordlund for their comments. I am grateful for Professor Srinivasan G. Srivilliputhur for his efforts as the opponent.

I would like to express my gratitude to Research Foundation at Lappeenranta University of Technology, Wihuri foundation, Academy of Finland, and TEKES for financial support.

Finally, I would like to thank my wife, Mari, for her support and encouragement over the years.

Lappeenranta, Aug 2010

Heikki Pitkänen

List of Publications

This thesis consists of an overview and the following publications

I A. Puisto, H. Pitkänen, M. Alatalo, S. Jaatinen, P. Salo, A. S. Foster, T. Kangas, K. Laasonen, Adsorption of atomic and molecular oxygen on Cu(100), Catal. Today 100, 403 (2005).

II M. Alatalo, A. Puisto, H. Pitkänen, A. S. Foster, K. Laasonen, Adsorption dynamics of O_2 on Cu(100), Surf. Sci. 600 1574-1578 (2006).

III T. Kangas, N. Nivalainen, H. Pitkänen, A. Puisto, M. Alatalo, K. Laasonen, Oxygen induced segregation of copper to Ag/Cu(100) surface, Surf. Sci. 600, 4103 (2006).

IV H. Pitkänen, A. Puisto, M. Alatalo, M. Ropo, K. Kokko, M. P. J. Punkkinen, P. Olsson, B. Johansson, and L. Vitos, Ab initio study of the phase stability in paramagnetic duplex steel alloys, Phys. Rev. B 79, 024108 (2009).

Authors contribution. In publications I and II the author has actively participated in the simulations, analysis of the results, and writing the papers. In publication III the author has participated in the analysis and writing. In publication IV the author has performed all the computations, and actively participated in interpreting the results and writing the paper.

Other relevant papers by the author, related to the present thesis.

V T. Kangas, K. Laasonen, A. Puisto, H. Pitkänen, M. Alatalo: On-surface and sub-surface oxygen on ideal and reconstructed Cu(100), Surf. Sci. 584, 62 (2005).

VI E. Airiskallio, E. Nurmi, M. H. Heinonen, I. J. Väyrynen, K. Kokko, M. Ropo, M. P. J. Punkkinen, H. Pitkänen, M. Alatalo, J. Kollar, B. Johansson, and L. Vitos: Third element effect in the surface zone of Fe-Cr-Al alloys, Phys. Rev. B 81, 033105 (2010).

VII E. Airiskallio, E. Nurmi, M. H. Heinonen, I. J. Väyrynen, K. Kokko, M. Ropo, M. P. J. Punkkinen, H. Pitkänen, M. Alatalo, J. Kollár, B. Johansson, and L. Vitos, High temperature oxidation of Fe-Al and Fe-Cr-Al: The role of Cr as a chemically active element. Submitted to Corrosion Science (2010).

Abbreviations

$\mathbf{a}$	Acceleration
CPA	Coherent Potential Approximation
d	Differential operator
DFT	Density Functional Theory
E	Energy
e_{s}	Surface energy
EMTO	Exact Muffin Tin Orbital(s)
$\mathbf{F}$	Force
g	Green function
GGA	Generalized Gradient Approximation
$\hat{H}$	Hamiltonian operator
$\mathbf{k}$	Wave vector (in reciprocal space)
LEED	Low Energy Electron Diffraction
m	Mass
MBSS	Molecular Beam Surface Scattering
MD	Molecular Dynamics
ML	Monolayer
PES	Potential Energy Surface
$\mathbf{r}$	Position vector (in real 3-space)
$\mathbf{R}$	Position vector (in real 3-space)
STM	Surface tunneling microscopy
v	Potential
VASP	Vienna Ab-initio Simulation Package
XPD	X-ray Photoelectron Diffraction
ϵ_i	Energy of a single-electron orbital
ψ_i	Single-electron Wave function
μ	Chemical potential
Ψ	Manybody wave function
∇	Differential operator
$\hbar$	Planck constant
Ω	Volume

Contents

1 Introduction **13**

1.1 Motivation . . . 13
1.2 Functionalization of materials . . . 14
1.3 Theory on surface alloys . . . 14
1.4 Oxidation of metals . . . 16
1.5 Steels . . . 16

2 Computational Methods **19**

2.1 Density Functional Theory . . . 19
2.1.1 Hohenberg-Kohn theorems . . . 20
2.1.2 The Kohn-Sham Ansatz . . . 21
2.2 Plane Wave Method . . . 23
2.3 Pseudopotentials . . . 26
2.4 Molecular dynamics method . . . 27
2.5 Exact Muffin Tin Orbitals Method . . . 28
2.5.1 Full Charge Density Method . . . 30
2.5.2 Coherent Potential Approximation . . . 31
2.6 Comparison of the methods . . . 32

3 Results **33**

3.1 Ag doped Cu surface . . . 33
3.1.1 O_2 adsorption . . . 33
3.1.2 Oxygen induced segregation of Ag/Cu . . . 38
3.2 FeCrNi duplex steels . . . 41

4 Concluding remarks **47**

REFERENCES . . . 49

Chapter 1

Introduction

1.1 Motivation

In the course of human cultural evolution, major paradigm shifts in the technological and socioeconomic development have marched hand in hand with those of materials science. The time when human cognition rose to such level that we can talk about technology, albeit primitive, is referred to as the stone age. Early humans learned that with certain techniques, tools and weapons that rise the odds of one's own survival, and those of one's family or tribe, can be constructed from the materials available; stone, wood and bone. Different types of rock could be used for different purposes, and that can be seen as primitive material technological research.

As the time when stone was the most important material of which early humans constructed their tools is referred to as the stone age, so are all prehistoric ages referred to by the material which dominated human life. After the invention of fire, early man learned to refine bronze from certain ores. The relics of bronze age prove that although many of the items found were utilitarian in nature, many were ritual artefacts. These ritual artefacts were connected to the dominant form of religious activity of bronze age, totemism. Totemism and it's rituals led way to mysticism and religions, which are argued to be a key component in the birth of cultures, and a major influence leading to increased social activity. [1]

The discovery of smelting and forging iron lead to the agricultural revolution. This in turn made it possible for big cities to be built, thus leading way to academia as we know it. Alchemy of those times evolved into modern chemistry, bringing the industrial revolution, and just a few centuries after that the last important paradigm shift manifested, bringing us the computer age. The rest, as they say, is history, and this is where we are now; materials science of our time has at it's disposal vast computational resources, and fast communication via the internet, making it possi-

ble for scientists to talk about hot topics of the day with virtually zero delay.

1.2 Functionalization of materials

Discoveries in the fields of nanoclusters and thin films have shown us that the size (when it is atomistic in scale) of an object affects its electrical, chemical and magnetic properties so much that we can think of the size of a nanocluster or the thickness of a thin film as a third axis perpendicular to those two in the periodic table. When we add to this the fact that we can alloy different elements together and construct composite objects (such as carbon nanotubes on a metal oxide substrate, which then works as a catalyst), the possibilities seem almost infinite. This is why theoretical understanding of the phenomena in atomistic size scales (nanometers) and timescales of tens of femtoseconds is needed in order to make the functionalization of such applications possible.

This is why *ab initio* computational methods, that have risen as the third important approach in physics, along theory and experiments, are so invaluable; theories cannot penetrate such complexity, and experiments can be measured in the timescales of microseconds, at best. Also, there is information available one can see in an *ab initio* simulation that is not visible in experiments, such as the electronic states of every single electron.

Although this work is not directly related to complex functionalized systems, the understanding this work provides adds understanding to the vast question portrayed above. For example, in the engineering of thin films one has to understand how the deposited material behaves on the substrate. When dealing with nanoclusters or porous materials, understanding how the surface energy of the material changes as a function of alloy composition or other factors is of crucial importance. Duplex steels, a part of this thesis, have a very peculiar microstructure, and can be seen as a functionalized material in their own right.

1.3 Theory on surface alloys

When metal is deposited on the surface of another metal, there are several possible ways for it to react, depending on the species of the metals. The impurity atoms may reside in the surface layer or have a tendency to diffuse further into the bulk, and they may form separate islands or a pseudomorphic alloy. It has to be mentioned here that the entropy driven diffusion of the impurity atoms towards the bulk

is usually very slow, and thus, in the time scale of oxidation phenomena, we can assume the surface to be in an equilibrium state.

By measuring a characteristic called the surface energy curve the metal surface alloys can be divided into four generic classes [2]. Figure 1.1 shows examples of the four generic classes.

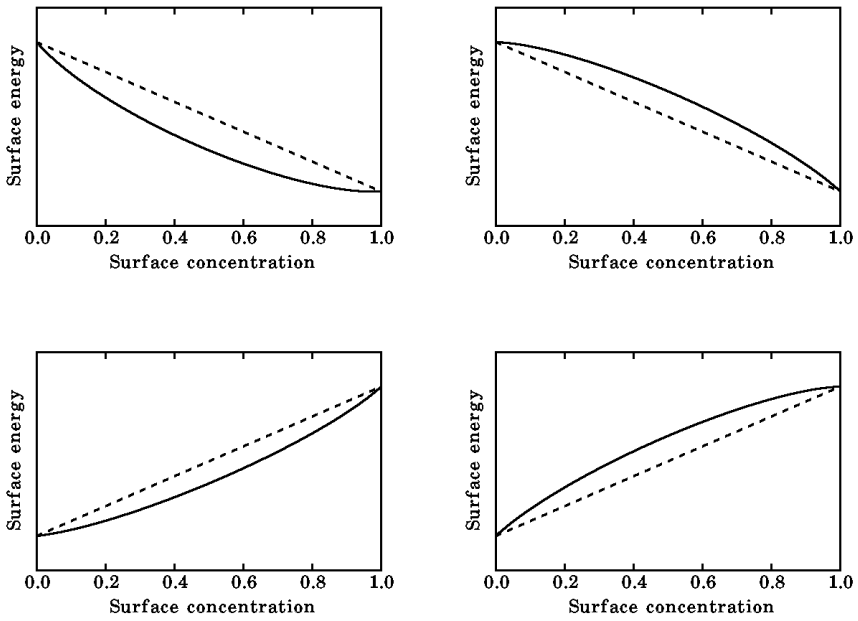

Figure 1.1: Schematic examples of the surface energy curves of all four generic classes. (Surface energy per substrate atom versus the concentration x of the deposited adatom.)

The upper row of Fig. 1.1 stands as an example of cases where the segregation energy is negative, $\mathrm{d}e_\mathrm{s}/\mathrm{d}x < 0$. The term $e_\mathrm{s} = e_\mathrm{s}(x)$ is the surface energy per surface atom and x is the percentual amount of admetal on the surface. In this case the deposited material stays in the surface layer. The lower row shows a case where the segregation energy is positive, $\mathrm{d}e_\mathrm{s}/\mathrm{d}x > 0$. In this case the deposited material will eventually dissolve into the bulk. Another feature the surface energy curve possesses is its curvature, which expresses the excess interactions between the adatoms. "Excess interactions" means interactions beyond that in an ideal solution, where all atomic arrangements (alloyed or dealloyed) are equally stable. A straight line connecting the surface energy of the clean surface ($x = 0$) and that of a monolayer of deposited material ($x = 1$) represents the ideal solution behavior with no excess interactions between the adatoms. This is seen in Fig. 1.1 as a broken line. The difference between the straight line and the actual curve is the mixing energy

of the random surface solution. When this is negative, corresponding to repulsive excess interactions between the adatoms, surface alloying, stable or metastable, occurs. The left column of Fig. 1.1 stands as an example of these occasions. When the mixing energy is positive, corresponding to attractive excess interactions between the adatoms, phase separation occurs. This means the adatoms form islands rather than forming a surface alloy. The surface energy curve of this kind of surfaces is seen in the right column of Fig. 1.1.

1.4 Oxidation of metals

Understanding of the nature of oxidation of metals has increased notably in recent years, owing to the contributions of a large number of investigators, both experimental and theoretical, who have provided a large quantity of information on this complex subject. Increase in computational power has made it possible for these phenomena to be studied via simulations, and since the automotive industry started to supply cars with catalysators to reduce monoxide emissions, there has been a drive to develop a more efficient catalytic materials. Since in many cases it is not the metal that works as a catalyst, but the metal oxide [3], the theoretical understanding of the oxidation of metals is of crucial interest from this viewpoint, too. Another industrial application that increases interest towards theoretical understanding of metal oxidation, is the future prospect of manufacturing better corrosion resistant materials.

Oxidation of a solid metal surface almost always starts with what is referred to as *initial oxidation*, that is, chemisorption/physisorption of O_2 molecules to the surface. After that, different kinds of surface oxides are formed. Then, the oxides assume a macroscopic structure, the form and geometry of which depends the metal and surface structure. For example, in the case of aluminum, a protective layer of oxide is formed on top of the metal surface, that protects it against further oxidation. Then again iron is known to rust, which means that over time, the oxide layer penetrates further and further into the bulk. As iron oxide is very brittle compared to iron, objects made of iron often disintegrate if left to rust long enough.

1.5 Steels

Steels are alloys that consist mostly of iron, and usually contain 1...2 atomic percent carbon, depending on the grade. Carbon is the most common alloying material for iron, but various other alloying elements are used. Varying the amount of alloying elements, along with various ways of heat treatment, one can control qualities such as the hardness, ductility, tensile strength, corrosion resistance, and electrical prop-

erties of the resulting steel. Steels can assume various phases (ferrite, cementite, austenite, pearlite, bainite, martensite and ledeburite), but for practical uses, they are usually categorized based on their properties, that is, their potential uses. A class of steels that is widely used in industry is carbon steels. These grades have very little other alloying species than carbon. These grades are normally not *stainless*. These grades are used in industry, because they are hard and strong, but their downside is their poorer ductility, and the fact that they are difficult to weld.

One of the best known classes of steels are stainless steels. They are an important and widely used family of engineering materials, due to their desired characteristics, the most important of which is their resistance to corrosion. Other desired characteristics include low maintenance, relatively low cost and antibacterial properties. Stainless steels also stay lustrous for a very long time, making them an attractive choice for architects and jewelers. The main stainless groups are austenitic and ferritic steels [4]. Stainless steels always contain minimum of 11% chromium content by mass. When the Cr content of a steel exceeds this limit, a passive film of chromium oxide is formed when the steel oxidizes. This oxide film prevents further surface corrosion and blocks corrosion from spreading into the metal's internal structure.

Maraging steels are iron alloys that possess superior strength and toughness without losing malleability. Maraging steels are strong, but unlike carbon steels, they do not derive their strength from carbon, but from intermetallic precipitates, the most important of which is nickel. All maraging steels contain 15 to 25% nickel. Other alloying elements include cobalt, molybdenum, and titanium.

Chapter 2

Computational Methods

For the first part of this thesis, which involves the oxidation of Ag/Cu(100) surfaces, we used the Vienna Ab-initio Simulation Package (VASP) [5, 6, 7, 8], with Vanderbilt ultrasoft (US) pseudopotentials [9]. For the second part, about paramagnetic duplex steel alloys, we used the Exact Muffin Tin Orbitals (EMTO) method [10, 11, 12], implemented with the Coherent Potential Approximation (CPA) [13, 14]. In this chapter both methods are presented and discussed.

In *ab initio* computational methods, one has to find the equations that govern the behaviour of the system, namely, the electrons and the nuclei. The first approximation almost all methods employ is to decouple the equations of motion of the atomic nuclei from those of the electrons (Born-Oppenheimer approximation) [15]. Since the mass of the ion cores is about three orders of magnitude greater than the mass of an electron, this approximation is well justified. One can then solve the electronic system separately in the Coulomb potential of the fixed nuclei, treating that potential as external to the system.

2.1 Density Functional Theory

Let us examine a system of N electrons in an external potential $V_{\text{ext}}(\mathbf{r})$. According to the postulates of quantum mechanics, all properties of a stationary system can be deduced from the Schrödinger equation

$$\hat{H}\Psi = E\Psi, \tag{2.1}$$

where $\hat{H}$ is the Hamiltonian operator, Ψ is the many-body wave function with all the particle coordinates as variables and E the total energy of the system. The Hamiltonian operator of the (electronic) system can be expressed as

$$\hat{H} = -\frac{\hbar^2}{2m}\sum_i \nabla_i^2 + \sum_i V_{\text{ext}}(\mathbf{r}_i) + \frac{1}{2}\sum_{i\neq j}\frac{e^2}{|\mathbf{r}_i - \mathbf{r}_j|} \tag{2.2}$$

where the first term gives the kinetic energies of the electrons, $V_{\text{ext}}(\mathbf{r}_i)$ is the external potential, and the last term includes all electron-electron interactions. There are methods that use the wave functions of electrons as their basic variables, and use the variational principle to solve them. The Hartree and Hartree-Fock methods [16] are the first ones of that kind, but due to their simplicity they fail to reproduce the physical phenomena they are meant to model in many cases, and therefore they are quite rarely in use. There is a group of so-called *post-Hartree-Fock methods* that are based on the Hartree-Fock formalism, but which due to certain additional corrections serve better as a simulation model. One such method is the configuration interaction method, in which different electronic states are mixed together, which is mathematically done by using linear combinations of Slater determinants. Another important method of that kind it the Møller-Plesset perturbation method [17]. It improves on the Hartree–Fock method by adding electron correlation effects by means of Rayleigh–Schrödinger perturbation theory [18] [19]. The abovementioned methods are rarely used in larger physical simulations, due to the long CPU time and immense hardware required for the calculations.

2.1.1 Hohenberg-Kohn theorems

The success of Density Functional Theory (DFT) begun when Hohenberg and Kohn suggested in 1964 that the many-body wave function was altogether too complicated an entity to be dealt with according to the methods of the variational principle. They theorized and later, in their work [20], proved that another, much simpler entity can be chosen for the basic variable: the *electron density which minimizes the total energy*. The fundamental tenet of density functional theory is that the many-body wave function, and therefore all properties of the system, are exactly defined by the electron density of the system. This means that if the ground state electron density is known, everything else can be defined as an exact functional of the electron density. This means an enormous simplification of the problem, because instead of the many-body wave function $\Psi(\mathbf{r}_1, \mathbf{r}_2, \cdots, \mathbf{r}_N)$, which is a function of $3N$ variables, we only need to solve the ground state electron density $n_0(\mathbf{r})$, a function of 3 variables.

The original works by Hohenberg and Kohn [20] and of Mermin [21] proved that the ground state electron density can be used as the basic variable, but they provide no means for calculating it. If it were not for the work of Kohn and Sham, the whole of density functional theory would have most likely remained no more than a curiosity.

2.1.2 The Kohn-Sham Ansatz

It is impossible to analytically solve the electronic density of a system of many atoms, so once again, we have to change the question. The idea of the Kohn-Sham theorem [22] is to replace the difficult interacting many-body system obeying the Hamiltonian with a different *auxiliary system* that can be solved more easily. This leads to independent-particle equations for the non-interacting system with all the difficult many-body terms incorporated into an *exchange-correlation functional of the density*. Thus the total energy of the original system can be calculated in three parts: One is the kinetic energy of the non-interacting electrons, one is the external potential (created by the ion cores) and the remainder term called the *exchange-correlation energy* which incorporates all many-body effects.

Kohn and Sham postulated that the total energy of the electronic system $E_e[n(\mathbf{r})]$ could be written in the form

$$E_e[n(\mathbf{r})] = T_s[n(\mathbf{r})] + E_{\mathrm{H}}[n(\mathbf{r})] + E_{\mathrm{XC}}[n(\mathbf{r})] + E_{\mathrm{ext}}[n(\mathbf{r})] \tag{2.3}$$

$$\begin{aligned} E_e[n(\mathbf{r})] = T_s[n(\mathbf{r})] &+ \frac{1}{2}\iint \frac{n(\mathbf{r})n(\mathbf{r}')}{|\mathbf{r}-\mathbf{r}'|}\mathrm{d}\mathbf{r}\mathrm{d}\mathbf{r}' + E_{\mathrm{XC}}[n(\mathbf{r})] \\ &+ \int n(\mathbf{r})V_{\mathrm{ext}}(\mathbf{r})\mathrm{d}\mathbf{r}, \end{aligned} \tag{2.4}$$

where $T_s[n(\mathbf{r})]$ is the kinetic energy of a system of non-interacting electrons, $E_{\mathrm{H}}[n(\mathbf{r})]$ is the classical Coulomb energy of the electron cloud, $E_{\mathrm{ext}}[n(\mathbf{r})]$ is the energy caused by the fact that electrons experience the external potential caused by the ion cores and other sources, and $E_{\mathrm{XC}}[n(\mathbf{r})]$ is the so-called exchange-correlation functional, a term that includes all electron-electron interactions beyond the Hartree term.

Now, to find the ground state of the system, we must find the minimum of $E[n(\mathbf{r})]$ with respect to n($\mathbf{r}$). We represent the electron density by a set of single electron orbitals $\{\psi_i\}$, as

$$n(\mathbf{r}) = \sum_{\epsilon_j \leq \epsilon_F} |\psi_i(\mathbf{r})|^2, \tag{2.5}$$

where the summation runs over all the Kohn-Sham states below the Fermi level ϵ_F, which in turn is obtained from the condition

$$N_e = \int n(\mathbf{r})\mathrm{d}\mathbf{r}, \tag{2.6}$$

where N_e is the number of electrons. Thus we end up having a set of single-electron equations

$$\left\{-\frac{\hbar^2}{2m_\mathrm{e}}\nabla^2 + v_\mathrm{eff}(\mathbf{r})\right\}\psi_i(\mathbf{r}) = \varepsilon_i\psi_i(\mathbf{r}), \tag{2.7}$$

where v_eff is the effective potential, defined as

$$v_\mathrm{eff}[n(\mathbf{r})] = v_\mathrm{ext}(\mathbf{r}) + v_\mathrm{Hartree}[n(\mathbf{r})] + \mu_\mathrm{XC}[n(\mathbf{r})], \tag{2.8}$$

where $v_\mathrm{Hartree}[n(\mathbf{r})]$ is the Hartree potential, defined by

$$v_\mathrm{Hartree}[n(\mathbf{r})] = 2\int \frac{n(\mathbf{r}')}{|\mathbf{r}-\mathbf{r}'|}\mathrm{d}\mathbf{r}' \tag{2.9}$$

and $\mu_\mathrm{XC}[n(\mathbf{r})]$ is the exchange-correlation potential defined as the functional derivative of $E_\mathrm{XC}[n(\mathbf{r})]$, as

$$\mu_\mathrm{XC}[n(\mathbf{r})] = \frac{\delta E_{XC}[n(\mathbf{r})]}{\delta n(\mathbf{r})}. \tag{2.10}$$

When the single-electron Schrödinger equations have been solved self-consistently, we can express the ground state energy of the electronic system as

$$E_e[n(\mathbf{r})] = T_s[n(\mathbf{r})] + \int v_\mathrm{Hartree}[n(\mathbf{r})]n(\mathbf{r})\mathrm{d}\mathbf{r} + E_\mathrm{XC}[n(\mathbf{r})] + \int v_\mathrm{ext}(\mathbf{r})n(\mathbf{r})\mathrm{d}\mathbf{r}, \tag{2.11}$$

where

$$T_s[n(\mathbf{r})] = \sum_{\epsilon_j \leq \epsilon_F}\int \psi_i^*(\mathbf{r})(-\nabla^2)\psi_i(\mathbf{r})\mathrm{d}\mathbf{r}. \tag{2.12}$$

It is worth noting that $T_s[n(\mathbf{r})]$ is not the kinetic energy of the interacting system. Rather, it is the kinetic energy of a non-interacting system with the same density, and as such, only helpful in the mathematical formulation of the system. The true kinetic energy can not be solved by this method.

If the external potential is only formed by fixed nuclei located on lattice sites $\mathbf{R}$ we have

$$v_\mathrm{ext}(\mathbf{r}) = -\sum_\mathbf{R}\frac{2Z_\mathrm{R}}{|\mathbf{r}-\mathbf{R}|}, \tag{2.13}$$

where Z_R are the nuclear charges. Having thus formulated the expression for the electronic energy functional, we can state the total energy of the system as

$$E_\mathrm{tot} = E_e[n(\mathbf{r})] + \sum_{\mathbf{R}\mathbf{R}'}\frac{Z_\mathbf{R}Z_{\mathbf{R}'}}{|\mathbf{R}-\mathbf{R}'|}, \tag{2.14}$$

where the last term is the nuclear-nuclear repulsion term.

All other terms in Eq. 2.3 can be explicitly defined, except for the exchange-correlation potential. The accuracy of DFT is therefore, in principle, limited only by the employed approximate functionals describing the exchange and correlation energies. Assuming a slowly enough varying potential, a series expansion of gradients can be constructed. If only the first term is taken into account and the rest omitted, the approximation is called the Local Density Approximation (LDA) [22]. Within the LDA, the exchange-correlation energy of an electronic system is constructed by assuming that the exchange-correlation energy per electron at a point $\mathbf{r}$ in the electron gas, $\epsilon_{XC}(\mathbf{r})$, is equal to the exchange-correlation energy per electron in a homogeneous electron gas that has the same electron density. This is expressed as

$$E_{XC}^{LDA}(\mathbf{r}) = \int \epsilon_{XC}(n(\mathbf{r}))n(\mathbf{r})d\mathbf{r}, \tag{2.15}$$

where $\epsilon_{XC}(n(\mathbf{r}))$ is the exchange-correlation energy per unit volume of a homogeneous electron gas of density n. If more terms are used beyond the first, the exchange-correlation potential is assumed not to be homogeneous, and gradient terms are included. These approximations are generally called Generalized Gradient Approximations (GGA) [23] [24] [25] [26].

It should be mentioned that the set of single-electron orbitals, $\{\psi_i\}$, in Eq. 2.5 can be represented in terms of any complete basis set, and several different choices are available. All basis sets have their strengths and weaknesses, and are best suited for certain types of problems. The choice of a basis set is a topic in itself, and it will be covered in more detail in the following section.

2.2 Plane Wave Method

In order to study a physical phenomenon, we construct a model of the desired situation for the simulation. Since the model cannot be of infinite size, it must have boundaries. Yet, the wave functions must be continuous, which means they cannot be terminated at those boundaries. For these reasons almost all *ab initio* methods designed to solve atomistic-scale phenomena employ *periodic boundary conditions*. The model under simulation is defined inside a *supercell*, which is a parallelepiped-shaped box. The periodic boundary conditions are such, that when a wave function exits the box on a certain facet, it re-enters the box on the facet opposing it. Another way of visualizing the situation is that we take the geometry defined inside the supercell, and then replicate it to fill all space. The model under simulation is of finite size, yet the wave functions stay continuous. This is useful in many aspects; we

can model bulk material with a rather tiny supercell (perhaps just one atom), but because of the periodic boundary conditions, the simulation is that of an infinitely large bulk. Similarly, we can define a surface slab of handleable size, which, by the replication of the supercell, simulates an infinitely wide surface. Another useful consequence is the fact that we can now employ the *Bloch Theorem* [27, 16].

Now, recall the single-electron Schrödinger equations (Eq. 2.7). We know that because of the periodic boundary conditions, the effective potential $v_{\text{eff}}(\mathbf{r})$ has the periodicity of the supercell, thus [27]

$$v_{\text{eff}}(\mathbf{r}) = v_{\text{eff}}(\mathbf{r} + \mathbf{R}) \tag{2.16}$$

where $\mathbf{R}$ is a vector of the form $\mathbf{R} = a_1\mathbf{x_1} + a_2\mathbf{x_2} + a_3\mathbf{x_3}$, the vectors $\mathbf{x_i}$ being the edges of the supercell, and a_i integers. Originally, the Bloch theorem was formulated for a perfect Bravais lattice, but we can write the eigenfunctions of the single-electron Schrödinger equations $\{\psi_i\}$ for any translationally invariant system in a fashion suggested by the theorem, thus:

$$\psi_{i,\mathbf{k}}(\mathbf{r}) = \mathrm{e}^{\mathrm{i}\mathbf{k}\cdot\mathbf{r}} u_{i,\mathbf{k}}(\mathbf{r}). \tag{2.17}$$

where $u_{i,\mathbf{k}}(\mathbf{r})$ are functions having the same periodicity as the effective potential, $u_{i,\mathbf{k}}(\mathbf{r}) = u_{i,\mathbf{k}}(\mathbf{r} + \mathbf{R})$, and $\mathbf{k}$ is any vector that lies within the first Brillouin zone. In a periodic DFT calculation, solutions of this form are applied to the Kohn-Sham equations. The problem was this far divided to N_e different equations (one for each electron); now, each of *them* is further divided to a set of equations, one for each $\mathbf{k}$-vector, or $\mathbf{k}$-point, as they are often referred to. One should note that the $\mathbf{k}$-vectors do not reside in real space, but in reciprocal space. One should also note that the label i, in italics, is the running index with which we refer to the i:th eigenfunction of the set $\{\psi_i\}$, whereas i, written with roman, is the imaginary unit.

Now, using the fact that any periodic function can be expanded in the complete set of Fourier components, we expand the function $u_{i,\mathbf{k}}(\mathbf{r})$ in Eq. 2.17 into a Fourier series, which gives

$$u_{i,\mathbf{k}}(\mathbf{r}) = \sum_{\mathbf{G}} c_{i,\mathbf{G}}\ \mathrm{e}^{\mathrm{i}\mathbf{G}\cdot\mathbf{r}}, \tag{2.18}$$

where $\mathbf{G}$ is a reciprocal lattice vector. By substituting this to Eq. 2.17, we can express an eigenfunction by expanding it, too, into a Fourier series, thus:

$$\psi_{i,\mathbf{q}}(\mathbf{r}) = \sum_{\mathbf{q}} c_{i,\mathbf{q}} \frac{1}{\sqrt{\Omega}} \cdot \mathrm{e}^{\mathrm{i}\mathbf{q}\cdot\mathbf{r}} \equiv \sum_{\mathbf{q}} c_{i,\mathbf{q}} \cdot |\mathbf{q}\rangle \tag{2.19}$$

where $c_{i,\mathbf{q}}$ are the (complex) expansion coefficients of the plane wave with the wave

vector $\mathbf{q}$ in the expansion of the Kohn-Sham orbital i. The symmetry label $\mathbf{q}$ is used in the equation for clarity, and it is simply $\mathbf{q} = \mathbf{k} + \mathbf{G}$. Ω is the volume of the supercell, and it is there in the equation because of normalization. The basis of plane waves $|\mathbf{q}\rangle$ is orthonormal, and they satisfy [28]

$$\langle \mathbf{q}'|\mathbf{q}\rangle \equiv \frac{1}{\Omega}\int_{\Omega} \mathrm{d}\mathbf{r} \cdot \mathrm{e}^{-\mathrm{i}\mathbf{q}'\cdot\mathbf{r}} \cdot \mathrm{e}^{\mathrm{i}\mathbf{q}\cdot\mathbf{r}} = \delta_{\mathbf{q},\mathbf{q}'}. \tag{2.20}$$

Now, inserting Eq. 2.19 into the set of single-electron Schrödinger equations (Eq. 2.7), multiplying from the left by $\langle \mathbf{q}'|$ and integrating as in Eq. 2.20 leads to the Schrödinger equation in Fourier space [28]

$$\sum_{\mathbf{G}} \langle \mathbf{q}'|\hat{H}_{\mathrm{eff}}|\mathbf{q}\rangle c_{i,\mathbf{q}} = \varepsilon_i \sum_{\mathbf{G}} \langle \mathbf{q}'|\mathbf{q}\rangle c_{i,\mathbf{q}} = \varepsilon_i c_{i,\mathbf{q}} \tag{2.21}$$

where

$$\hat{H}_{\mathrm{eff}} = -\frac{\hbar^2}{2m_{\mathrm{e}}}\nabla^2 + v_{\mathrm{eff}}(\mathbf{r}). \tag{2.22}$$

By expanding the effective potential v_{eff} as its Fourier components, thus

$$v_{\mathrm{eff}} = \sum_{\mathbf{G}} \tilde{v}_{\mathrm{eff}}(\mathbf{G})\ \mathrm{e}^{\mathrm{i}\mathbf{G}\cdot\mathbf{r}} \tag{2.23}$$

one finally arrives to the effective single-electron Schrödinger equation

$$\sum_{\mathbf{G}'} \left\{ \frac{\hbar^2}{2m_{\mathrm{e}}}|\mathbf{k}+\mathbf{G}'|^2\ \delta_{\mathbf{G},\mathbf{G}'} + \tilde{v}_{\mathrm{eff}}(\mathbf{G}-\mathbf{G}') \right\} c_{i,\mathbf{G}'}(\mathbf{k}) = \varepsilon_i(\mathbf{k})\ c_{i,\mathbf{G}}(\mathbf{k}). \tag{2.24}$$

One should note that there is now a separate equation for both every Kohn-Sham orbital i and every $\mathbf{k}$–point. Now, we can calculate the exact real space electron density as

$$n(\mathbf{r}) = \sum_{i=1}^{N} \frac{1}{\Omega}\int_{\Omega} |\psi_{i,\mathbf{k}}(\mathbf{r})|^2 \mathrm{d}\mathbf{k}. \tag{2.25}$$

Now, we have separated the equations so that we have a set of single-electron equations, one for each Kohn-Sham orbital i and one for each point in the reciprocal space, that is, every $\mathbf{k}$-point. All the mathematical steps this far have been very important, but the equations are not yet in such a form as to be helpful in numerical calculations. That is because of two reasons; first of all, the number of equations is infinite because we have an infinite number of Fourier components in the expansion of each Kohn-Sham orbital. Second, even when we reduce the number of required Fourier components for the Kohn-Shan orbitals with a technique that will be discussed shortly, the number of equations would still be infinite because we have an equation for each $\mathbf{k}$-point, and the set of $\mathbf{k}$-points in the reciprocal space is infinitely

dense.

We know that the Fourier components of the expansion of eigenfunctions have kinetic energy defined as [29]

$$E_{\text{kin}}(c_{i,\mathbf{k}}) = \frac{\hbar|\mathbf{k}+\mathbf{G}|^2}{2m_{\text{e}}}, \tag{2.26}$$

and we know, that the higher the kinetic energy of the term, the less significant it is in the representation of the eigenfunction. Based on this knowledge, so-called *cut-off energy* is defined, and all terms with kinetic energy greater than that are omitted. It is left for the scientist performing the calculations to define the appropriate cut-off energy, based on the criterion that the change in the total energy of the system is within an acceptable margin, when the rest of the terms in the series representation are omitted. We thus also know the magnitude of error this approximation generates to our calculations.

After the energy cut-off the single-particle orbitals ψ_i become finite, but the number of equations would still be infinite if we didn't quantize the volume. We can map the volume in reciprocal space where the calculation is done by a continuous set of points, $\{\mathbf{k} : \mathbf{k} = (k_x, k_y, k_z)\}$, throughout that region of reciprocal space. Now, since we know that wavefunctions at **k**-points that are very close together will almost be identical we can represent the electronic wavefunctions over a region of reciprocal space at a single **k**-point. This approximation allows us to calculate the electronic potential at a finite number of **k**-points. There are several ways to choose the **k**-point mapping. The most commonly used scheme is the one proposed by Monkhorst and Pack, where the **k**-points are distributed homogeneously in a three-dimensional grid [30]. All plane-wave calculations in this thesis employ the Monkhorst-Pack scheme.

2.3 Pseudopotentials

Developing accurate and at the same time efficient numerical methods for solving the Kohn-Sham equations has been among the biggest challenges within computational materials science, and as can be expected, one often has to make a compromise between accuracy and efficiency when choosing a method. When accuracy is essential, the method of choice is the full potential method. It includes all information of the electronic potential of atoms to high accuracy. The downside of this method is that the inclusion of the rapid oscillations in the wave function near the atomic nuclei makes this method numerically very cumbersome. Because of that, the method is used only if very high accuracy is needed. One of these uses is as a comparison when testing approximations.

A widely used approach in reducing the compulational burden of full potential methods is the pseudopotential method. If one were to construct a plane wave expression of the electron density of a real system, the amount of plane waves (Fourier components) needed for the representation of the density would be rather large due to the aforementioned rapid oscillations in the electronic states near the atomic nuclei, leading to heavy calculations. Fortunately, it has been shown that the core electrons of any atomic species are almost independent of the environment surrounding the atom, and that only the valence electrons participate strongly in the interactions between atoms. Thus, a pseudo wavefunction may be constructed, replacing the rapidly oscillating states near the atomic nuclei with a smooth electron distribution. The pseudo wavefunctions do not exhibit the rapid oscillations of the all-electron wavefunctions, dramatically reducing the number of plane waves needed for their representation, obviously resulting in smaller amount of computational effort needed for the calculation [31]. As schematically illustrated in figure 2.1, the all-electron wavefunction and the pseudo wavefunction coincide after a certain distance from the nucleus, noted r_c (core radius). Many types of pseudopotentials exist. To mention a few of the most widely used ones, they include norm-conserving pseudopotentials[32, 33, 34], ultrasoft (US) pseudopotentials [9], and the projector augmented wave (PAW) [35] which can be considered as a combination of pseudopotential and all-electron approaches.

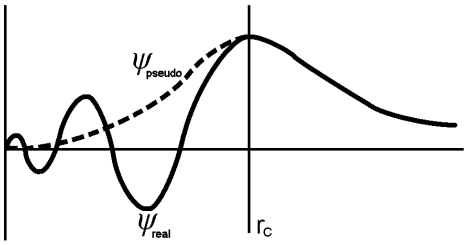

Figure 2.1: A schematic illustration of the wavefunctions corresponding to the all-electron potential and the pseudo-potential. Note that outside the core region the curves coincide.

2.4 Molecular dynamics method

The first principles molecular dynamics (MD) method [36] is an application of the Density Functional methods, which offers us the tool to study how a system evolves with time. In the MD method, each atom has initially not only it's position, but also it's velocity predetermined by the user. The user may also let the code give it an initial velocity, which is randomized within a thermal statistic. The evolution

of the system with time is calculated with discrete time steps, and it is left for the scientiest to make sure the time step is short ehough to prevent aliasing of the highest frequency molecular vibrations, but then again long enough that the simulation is not unnecessarily slow (simulating a time interval of 1 picosecond can take about a month of real time). The simulation progresses in this manner: the electron density is calculated using the pseudopotential method formalism, during which the atomic nuclei are not allowed to move. Then, we can determine the forces acting upon each of the atomic nuclei using the Hellmann-Feynmann theorem [28]

$$\mathbf{F}_i = -\frac{\partial E}{\partial \mathbf{R}_i}, \tag{2.27}$$

where E is the energy of the system, and $\mathbf{R}_i$ is the position vector of the atom in question. Then, we can determine the acceleration this force causes by the well-known Newton's second law

$$\mathbf{F}_i = m\mathbf{a}_i, \tag{2.28}$$

where m is the mass of the atomic nucleus in question. After that, the newly determined acceleration vectors are added to the velocity of each atom, and after this, the atoms move to the direction of their velocity vector, a length determined by the absolute value of the velocity, and the length of the time step. After the atoms have assumed their new positions, a new electron density is calculated using these positions, and so it continues. The MD simulation never reaches an end *per se*, it is left for the scientist to determine when the simulation has run long enough. Either one sees that the reaction one wished to simulate has happened, or it becomes evident it is not going to happen, and the system reaches a thermal steady state.

2.5 Exact Muffin Tin Orbitals Method

The third important group of Kohn-Sham methods, in addition to the full potential method and the pseudopotential method reviewed in the previous chapter, is built around the *muffin-tin approximation* to the effective potential and electron density [37]. This approximation is based on the observation that the exact crystal potential is atomic-like around the atom cores and almost flat between the atoms. In the light of this observation, muffin-tin methods substitute the Kohn-Sham potential with spherically symmetric potentials centered around the lattice sites and an almost flat potential in the interstitial region. When the Muffin Tin methods were first formulated, the division of space to atomic spheres and the interstitial region *did* look like a muffin tin, because the muffin tin wells were defined to be of such size that the muffin tin orbitals did not overlap (see Fig. 2.2). Nowadays, Muffin Tin methods usually employ *optimized overlapping muffin-tin* potentials, within which

the spherical regions around each lattice point around which the potential is defined are so large, that no space is left uncovered by them. These methods are referred as the *Exact Muffin Tin Orbitals* (EMTO) methods, the term "Exact" referring to the fact that the single-electron equations are solved exactly.

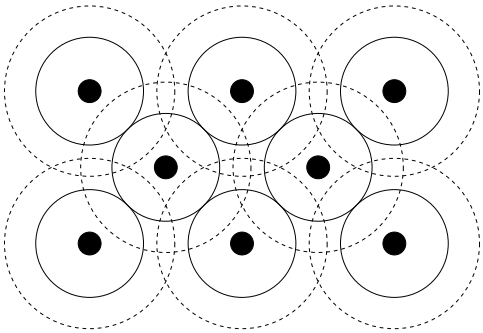

Figure 2.2: Space division to muffin tin spheres. The black dots denote the atomic nuclei, solid lines denote the non-overlapping muffin-tin wells of earlier muffin-tin methods, and dashed lines denote the optimized overlapping muffin-tin potentials.

The main difficulty in application of Density Functional Theory to real systems is related to the presence of various kinds of disorder. To calculate the energetics of a system containing chemical or magnetic disorder with a conventional DFT method, one would need to perform numerous calculations with very large systems. With the EMTO method, employing the Coherent Potential Approximation (CPA), we can instead of a large supercell, where the identity of each atom is specified, replace it with a much smaller one, containing a single pseudo-atom type. That pseudo-atom's characteristics are such, that it yields, on the average, the scattering properties of the alloy.

Within the overlapping muffin-tin approximation, the effective single-electron potential in Equation 2.8 is approximated by spherical potential wells $v_{\mathrm{R}}(\mathbf{r}_{\mathrm{R}}) - v_0$ centered on lattice sites $\mathbf{R}$ plus a constant potential v_0, as follows:

$$v(\mathbf{r}) \approx v_{\mathrm{mt}}(\mathbf{r}) \equiv v_0 + \sum_{\mathbf{R}} [v_{\mathrm{R}}(\mathbf{r}_{\mathrm{R}}) - v_0] \tag{2.29}$$

For clarity, here and from now on, vector notation $\mathbf{r}_{\mathrm{R}} \equiv \mathbf{r} - \mathbf{R}$ is used. By definition, $v_{\mathrm{R}}(\mathbf{r}_{\mathrm{R}})$ becomes equal to v_0 outside the potential sphere of radius s_R. For fixed potential spheres, both the spherical and the constant potentials from the right hand side of Equation 2.29 are determined by optimizing the mean of the squared deviation between $v_{\mathrm{mt}}(\mathbf{r})$ and $v(\mathbf{r})$, *i.e.* minimizing the

$$F_v[\{v_{\rm R}\}, v_0] \equiv \int_\Omega \left\{ v(\mathbf{r}) - v_0 - \sum_{\mathbf{R}} [v_{\rm R}(\mathbf{r}_{\rm R}) - v_0] \right\}^2 d\mathbf{r} \tag{2.30}$$

functional. Here Ω is the region where the potential optimization is performed. Since F_v is a functional of the spherical potentials, the minimum condition is expressed as

$$\int_\Omega \delta v_{\rm R}(\mathbf{r}) \frac{\delta F_v[\{v_{\rm R}\}, v_0]}{\delta v_{\rm R}(\mathbf{r})} d\mathbf{r} = 0 \quad \text{for any} \quad \mathbf{R} \tag{2.31}$$

where $\delta/\delta v_{\rm R}(\mathbf{r})$ stands for the functional derivative, and

$$\frac{\partial F_v[\{v_{\rm R}\}, v_0]}{\partial v_{\rm R}(\mathbf{r})} = 0. \tag{2.32}$$

The solution of these equations gives us the optimal $v_{\rm R}(\mathbf{r}_{\rm R})$ and v_0, and thus leads to the *optimized overlapping muffin-tin* potential. Having defined the potential, we can solve the single-electron equation (Equation 2.7) for the muffin-tin potential defined in Equation 2.29 by expanding the Kohn-Sham orbiltals $\psi_i(\mathbf{r})$ in terms of *exact muffin-tin orbitals* $\overline{\psi}^a_{\rm RL}(\epsilon_j, \mathbf{r}_{\rm R})$, *viz.*

$$\psi_j(\mathbf{r}) = \sum_{\rm RL} \overline{\psi}^a_{\rm RL}(\epsilon_j, \mathbf{r}_{{\rm R},v_0}) v^a_{{\rm RL},j} \tag{2.33}$$

The expansion coefficients, $v^a_{\rm RL}$, are determined from the condition that the above expansion should be a solution for Equation 2.7 in the entire space. The exact muffin-tin orbitals form a complete basis set for the Kohn-Sham problem. They are defined for each lattice site $\mathbf{R}$ and for each $L \equiv (l, m)$, where l is the orbital quantum number, and m is the magnetic quantum number.

2.5.1 Full Charge Density Method

The *Full Charge Density* (FCD) technique is developed as an alternative to full-potential methods, as it is highly efficient, and at the same time it gives total energies with an accuracy similar to that of full-potential methods. The Hohenberg-Kohn variational principle [20] states, that the total energy functional is stationary for small density variations around the equilibrium density. The FCD method is based on that notion, and the observation based on the fact, that any reasonably accurate trial density is suitable to determine the total energy of the system within an error which is second order in the difference between the trial and equilibrium charge densities.

The FCD method uses the total charge density to compute the total energy functional given by Equations 2.11 and 2.14. The total density is taken from the self-consistent calculation employing certain approximations. The energy components

from Equation 2.11 are calculated with the means of a *shape function*, which is a three-dimensional step function, defined so that is equals to 1 inside the Wigner-Seitz cell, and 0 otherwise. After the total charge density has been obtained from the self-consistent EMTO calculation, it is used to evaluate the total energy functional from Equations 2.11 and 2.14. The total energy functional is calculated as sum of a kinetic energy term T_s, an exchange-correlation energy term E_{XC}, and an electrostatic energy term E_c. The electrostatic energy is split into an intra-cell energy contribution functional F_{intra}, and an inter-cell energy contribution functional F_{inter}. Expressing the total density $n(\mathbf{R})$ as components defined inside the Wigner-Seitz cells, as

$$n(\mathbf{r}) = \sum_{\mathbf{R}} n_{\mathrm{R}}(\mathbf{r}_{\mathrm{R}}) \tag{2.34}$$

the FCD total energy functional is then be expressed as

$$E_{\mathrm{tot}} = T_s + \sum_{\mathbf{R}} (F_{\mathrm{intra}}[n_{\mathrm{R}}] + F_{\mathrm{XC}}[n_{\mathrm{R}}]) + F_{\mathrm{inter}}[n_{\mathrm{R}}]. \tag{2.35}$$

The mathematical formulations of the shape function and the abovementioned energy contributions are rather lengthy, and are not discussed here. An interested reader is referred to Ref. [38].

2.5.2 Coherent Potential Approximation

In substitutionally disordered alloys, any atomic site can be occupied by any of the atomic species in the system. As mentioned earlier, one method to perform calculations with such systems is to define a large supercell where the identity of each atom is specified. Such an approach is computationally very demanding, which is why alternative methods have been developed. Within the Coherent Potential Approximation [13, 14], the random array of real muffin-tin wells is replaced with an ordered array of effective wells. The scattering properties of the effective wells are then determined self-consistently, in a single-site mean-field sense, from the requirement that an electron traveling in an infinite array of effective wells undergoes, on average, no further scattering upon replacing one of the effective wells with one of the real potential wells [39]. When the scattering properties of an effective potential well are determined, quantities such as species-decomposed average density of states and charge density can be calculated straightforwardly [40].

Since the real potential wells are replaced with the effective ones, certain approximations are made. The first approximation is that the local potentials around a certain type of atom from the alloy are the same, *i.e.* the effect of local environments are neglected. Second, the system is replaced by a monoatomic set-up described by the

site independent *coherent potential* [38].

2.6 Comparison of the methods

It is obvious from the fact that several methods exist and are still in use, that certain methods are better suited for certain types of problems than others. In this section, the strengths and weaknesses of the Plane Wave method and the Muffin Tin method are compared. One distinct shortcoming of the Muffin Tin method is that the potential wells are defined, by the mathematics that define the method, to be located on the lattice points of a perfect lattice. This means that the Muffin Tin method is not suited for the kind of calculations performed for the copper surface studies of this thesis, because those calculations require that the atoms can be positioned freely. One can, though, use the Muffin Tin method to model such situations as surfaces or vacancies, because even though atoms must be positioned to the lattice sites of a perfect lattice, one can leave a lattice site empty (it is then occupied by an "empty sphere").

As mentioned above, the power of the EMTO-CPA method is that it can take several types of disorder into account by employing the Coherent Potential, and thus simulate, with a rather small computational burden, situations which would take huge computer resources if simulated by a pseudopotential method. Each pseudo-atom in the CPA formalism can be defined to have different ratios of each element, which makes it possible for one to study rather complex problems, for example surface segregation profiles.

In the next chapter, the obtained results will be shown and discussed. As can be guessed at this point, both of the methods introduced above have been used. The other part of of my studies dealt with oxidation of Cu surfaces, and how doping the surface with Ag affects the oxidation kinetics. Due to the kind of problem at hand, the pseudopotential method was an excellent choice for the case. To see how the surface reacts to oxygen, the atoms must have unlimited freedom to move along all 3 coordinate axes, and thus the EMTO method could not be used for this type of problem. The next part of my studies was about FeCrNi steels, the bulk properties of an interesting composition called "duplex steel" versus alloy composition. As mentioned in the previous paragraph, to do this kind of study without immeasurable computational resources, a conventional method like the pseudopotential method can not be used. Instead, the CPA implemented within the EMTO code enables us to do these studies.

Chapter 3

Results

3.1 Ag doped Cu surface

3.1.1 O_2 adsorption

Studying the chemical reactions on doped metal surfaces is important in many respects. The understanding of surface phenomena on atomistic length and time scales could bring a myriad of new technology, including corrosion free materials with desired electric and magnetic properties. Since it has been shown that on some transition metal surfaces the catalytic reactions actually occur due to oxidation [3], understanding these processes could enable us to develop materials with unique catalytic properties. As both Cu and Ag are widely used materials, Ag/Cu is a reasonable choice as an alloy whose behaviour to study, thus widening the collective understanding of surface phenomena. As Cu is an important material in electronics industry, and as electronic components are reaching the nanoscopic scale, the atomistic-scale understanding of the reactivity of Cu has a special interest.

A reaction which is of great interest in electronics is oxidation, since the conductivity properties of copper reduce dramatically due to oxidation. Since it is known that when Ag is deposited on a Cu surface, it forms an Ag film over the Cu, rather than forming an alloy [41], one could assume Ag deposition to be a relatively easy way of producing corrosion free copper components. However, the O_2 exposure study of Hirsimäki *et al.* [42] showed that 1 ML Ag has an almost vanishing effect on the oxidation rate of Cu(100) in large timescales (5 minutes). Also the molecular beam surface scattering (MBSS) study by Junell *et al.* [43] showed that the presence of 0.9 ML Ag on the surface has very little effect on the oxidation kinetics of Cu(100). As one can not extract data on atomistic length or time scales from these studies, it is important to study the phenomenon further. DFT simulations provide a complementary means of doing that.

It has been observed with X-ray photoelectron diffaction (XPD) and low energy electron diffraction (LEED) studies [41] as well as scanning tunneling microscopy (STM) studies [44] that when Ag is adminstered on a Cu(100) surface, the Ag atoms first take places within the topmost Cu layer (a surface alloy is formed). As the amount of Ag on the surface layer exceeds 0.13 monolayers (ML), the strain energy induced by the alloyed Ag becomes so high that the Ag atoms segregate into small patches of $c(2 \times 10)$ superstructure located within the surface layer. As the amount of Ag reaches 0.9 ML, a complete pseudo (111) overlayer is formed.

In order to study a case where there is a $c(2 \times 10)$ overlayer of Ag on top of a Cu substrate, with the thickness of the sample slab large enough as to represent the surface of a large object (rather than a thin film) adequately, the number of atoms per supercell would get so high that the simulation would be computationally impossible with this method. Therefore we have restricted ourselves to cases where the concentration of Ag atoms in the surface is under 0.13 ML, which means the Ag atoms form a surface alloy with the surface Cu atoms (there is no island formation). This way, we can use supercells which are a fraction of the size required for simulations with the overlayer, thus making it possible to perform the simulations with realistic computational cost and time.

Fig. 3.1 is a schematic figure reproduced from the MBSS results of Junell *et al.*. They discovered in their experiment a rather surprising outcome to the situation where O_2 is arriving onto a Cu(100) sample which is coated with 1 ML of Ag: contrary to what one might suppose, the presence of a monolayer of Ag has very little effect to the initial sticking coefficient.

In order to begin tackling the problem, potential energy surfaces (PES) were calculated for several different orientations. In order to plot a potential energy surface, one calculates a series of static simulations (atoms are frozen to their predetermined places and not allowed to move) of a geometry where, in our case, there is an O_2 atom over a Cu(100) surface, and for each simulation the distance of the O_2 molecule from the surface, or the interatomic distance between the O_2 molecules, is varied. In this manner, one ends up with a table of total energies of the system, and can thus plot a figure where one axis is the interatomic distance between the O_2 atoms, and the other is the distance between the surface and the O_2 molecule.

Although PES plots are a good way to visualize the possible existence and characteristics of an entrance channel, one should bear in mind that there are lots of phenomena that PES plots do not show, and the PES plots can be misleading if one is not aware of these "hidden" phenomena. One obvious phenomenon that is omit-

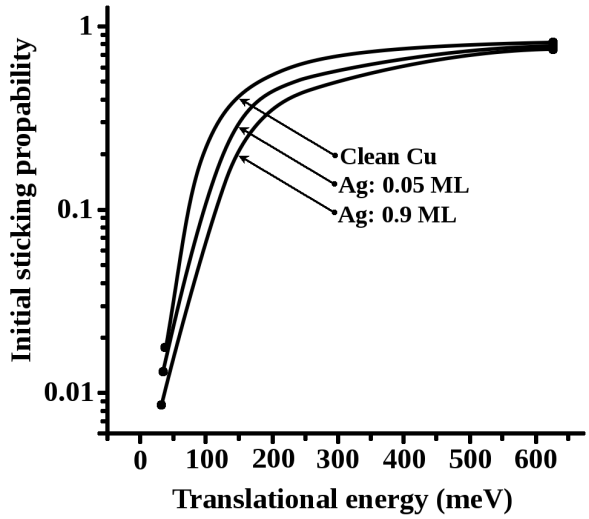

Figure 3.1: Schematic figure representing how surface modification with varying amounts of Ag affect the inital sticking probability of O_2 arriving on Cu(100). This figure is reproduced from [43].

ted from these simulations is the restructuring of surface geometry caused by the kinetic impact of the molecule. These deformations can be surprisingly strong, as we noticed in molecular dynamics (MD) simulations (these will be discussed shortly in more detail). Another blind spot of PES simulations is the fact that a molecule that is coming to the surface has, of course, many geometrical freedoms that are not present in the PES plot. The PES plot only takes into account its movement perpendicular to the surface and the stretching of its interatomic distance, but in addition to these the molecule can steer to some other location on the surface (move parallel to the surface), and it can also change it's orientation (rotate). The PES plots are, however, a very usable tool when searching the most interesting orientations, which can then be further studied with more accurate, but more computationally costly methods, such as the aforementioned molecular dynamics method.

We calculated such plots for several different geometries, two of which are shown in Figs. 3.2 and 3.3. Fig. 3.2 depicts a situation where an O_2 molecule is approaching the top site of a Cu atom, and the surface in question is a clean Cu(100) without any modifications. Fig 3.3 depicts a similar situation, but with one of the nine surface Cu atoms replaced with an Ag atom, the O_2 molecule in question approaching it

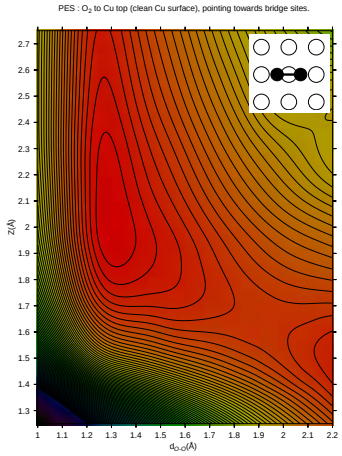

Figure 3.2: O_2 to Cu top (clean Cu surface), pointing towards bridge sites. Line separation is 0.2 eV.

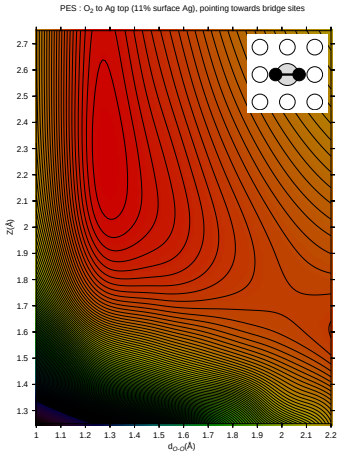

Figure 3.3: O_2 to Ag top (11 % Ag), pointing towards bridge sites. Line separation is 0.2 eV.

(see the small schematics in the top right corners of the PES images). In both cases, the orientation of the O_2 molecule is such that it is parallel to the surface, and it has its O atoms pointing towards the nearest bridge sites.

Now, what can we see from these figures? Looking at the entrance channel of Fig. 3.2 we can see that in order for the molecule to dissociate, it will need the kinetic energy of around 0.4 eV. This can be seen in the figure as follows: there are 5 lines to cross when crossing through the dissociation barrier, which means the "cost" in energy of $5 \cdot 0.2$ eV. But as there are also 3 lines crossed when entering the entrance channel, the energy gained this way is $3 \cdot 0.2$ eV. In other words, one only needs to count the non-closed circles from the dissociation barrier, and thus determine the cost in energy. Following similar logic, we can tell that the cost in energy for an O_2 atom to dissociate in the case where it is approaching the top site of the Ag impurity atom is 1.6 eV. That is 1.2 eV higher than in the case of clean Cu, and from this we can deduce that Ag strongly inhibits dissociative chemisorption of O_2 to the surface.

We also calculated a case like the one in Fig. 3.3, with the only difference that the orientation of the O_2 molecule was such that the O atoms were pointing to nearest hollow sites. The PES of that case was almost identical to Fig. 3.3. We also calculated the PES of a geometry where the O_2 molecule was approaching a Cu atom diagonally adjacent (that is, as far as possible in this geometry) to the Ag atom, the O atoms pointing to the nearest hollow sites. The PES of this case was practically identical to that of the clean Cu surface. From this we can deduce that

the presence of Ag on the surface has no effect on that range.

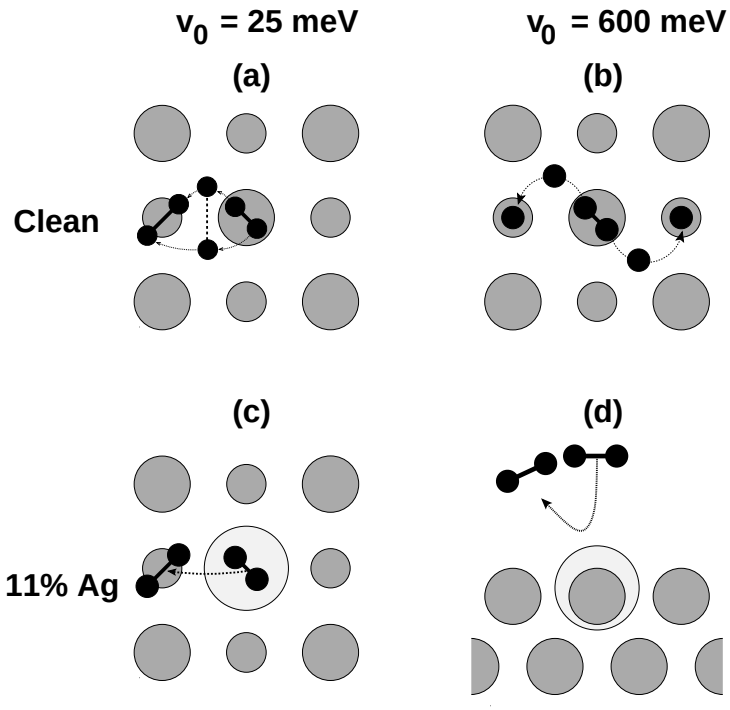

Figure 3.4: Schematic figures of how the molecular dynamics runs progressed. The upper row (a and b) represent the cases of clean Cu surface, and the lower row (c and d) depicts the cases with 11% ML of Ag on the surface. The small black spheres represent O atoms. The gray circles represent Cu atoms: in figures a, b, and c, the larger gray circles represent Cu atoms in the first layer, and the smaller ones represent Cu atoms in the second layer. Figure d is wieved from the side. The large light gray circles represent Ag atoms. The figures in the left column, (a and c), represent the cases where the initial velocity of the oxygen molecule was 25 meV, and the right column represents the case where it was 600 meV.

Having simulated and interpreted the PES results, we chose the most important cases for further study, and complemented the research with a more precise but computationally costy method, the first principles molecular dynamics (MD) method. We used a supercell with 9 surface atoms, and 6 layers thick. The initial state of all atoms was determined as follows: the oxygen molecule had a predetermined kinetic energy downwards (towards the surface), whereas the surface atoms had their velocities and initial directions randomized according to the thermal statistic, corresponding to the thermal motion at the temperature of 300 K. We simulated the cases for which the PES plots are shown, both of them with two different energies,

to see how the kinetic energy of the arriving oxygen molecule affects the dynamics.

Let us first have a look on the cases where the surface in question is a clean Cu surface (the upper row of Fig. 3.4). In the case where the initial velocity of the O_2 molecule was 25 meV, the molecule first approaches the surface, and having reached a certain distance it starts to steer away from the top position. As this happens, the O atoms move further apart from each other, and it is a matter of definition whether one can call it a molecule at this point. However, the stretched molecule then moves on top of the nearest hollow site, and there the interatomic distance between the O atoms shrinks back, and the molecule stays there, in a molecular precursor state. Molecular adsorption could also be predicted from the PES plots; one can imagine that the energy minima that are present in both the displayed PES plots attract the molecule, and thus the molecule is not necessarily dissociatively adsorbed, nor does it necessarily scatter back.

When we increased the initial velocity of the oxygen molecule to 600 meV, the system behaved quite differently. The molecule approached the surface Cu atom, pushed it down about a quarter of a lattice parameter, and after that the molecule split. As indicated by the arrows in the figure, the O atoms, after the molecule split, took their initial directions towards the nearest bridge positions, then changed their direction, and then stayed in the nearest hollow sites on both sides of the top site which they initally approached.

With silver present, the low-energy case is very similar to the corresponding case with a clean Cu surface. Even if the PES shows that direct dissociative adsorption is strongly inhibited, it cannot tell whether the molecule will steer away from its initial orientation. As one of the PES results showed, the presence of Ag on the surface does not have a long-range effect, and thus it is no surprise that this kind of dynamics might exist. The high-energy case with Ag/Cu surface showed a rather interesting case: the kinetic impact of the arriving oxygen molecule pushed the Ag atom over half a lattice parameter's length downwards (towards the bulk) after which the Ag atom springed back up, pushing the oxygen molecule further away, thus casting the oxygen molecule back to the gas phase.

3.1.2 Oxygen induced segregation of Ag/Cu

Hirsimäki *et al.* discovered in their Ag/Cu oxygen exposure experiment [42], that oxidation of Cu(100) is strikingly similar to that of Cu(100) with an Ag overlayer on top of it. This experiment, indicates that this is due to a rapid oxygen induced segregation of Cu to the surface and subsequent formation of Cu oxider on top of the Ag overlayer. To study the observed phenomenon using first-principles methods,

a series of relaxation runs were performed. Fig. 3.5 depicts a schematic of the geometries used for the simulations. We used a slab which was 5 atomic layers thick, and 2×2 conventional unit cells wide. In all simulations, one of the Cu layers was replaced with an Ag one, and the location of the Ag layer was varied. The Ag layer resided either on top of the Cu slab, in the second layer, or in the third layer. For each location of the Ag layer, five different oxygen coverages were simulated: 0, .25, .50, .75 and 1 ML. For comparison, we also calculated a case where there is no Ag in the slab, but only clean Cu. As the lattice constant in all calculations, we used the lattice constant of clean Cu. One must note that this choice of geometry causes strain in the Ag layers, as Ag normally has a lattice constant 13% larger than Cu. We decided this to be a reasonable choice however, since the strain is equal in all geometries, and thus cancels itself out when we compare the relative energetics of these systems. After the simulations, we calculated surface energies for each geometry as follows:

$$E_{surf} = E_{O/Cu/Ag} - N_{Cu} \cdot E_{bulk}^{Cu} - N_{Ag} \cdot E_{bulk}^{Ag} - N_O \cdot \frac{E_{O_2}}{2} - E_{surf}^{bottom}, \qquad (3.1)$$

where $E_{O/Cu/Ag}$ is the total energy of the Ag/Cu surface with O on it (the geometries depicted in Fig. 3.5), E_{bulk}^{Cu} and E_{bulk}^{Ag} are the energies of a single metal atom in bulk with its equilibrium lattice constant, E_{O_2} is the energy of an oxygen molecule and E_{surf}^{bottom} is the surface energy of the "bottom side" of the simulated slab.

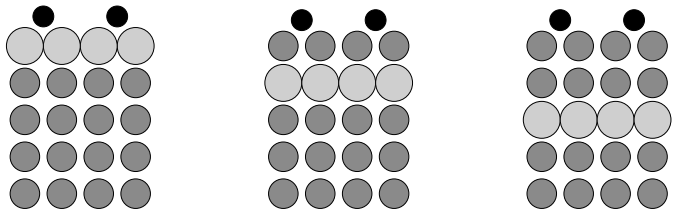

Figure 3.5: Schematic figure representing the atomic orientations used in the segregation simulations. The smaller gray spheres represent Cu atoms, larger light gray spheres represent Ag atoms, and the small black dots represent O atoms. Note that with each geometry five different oxygen coverages were simulated: 0, .25, .50, .75 and 1 ML.

Now, let us plot the energetics in order to have an intuitive view on how the energetics behave. In Fig. 3.5 we have plotted the surface energies in two different ways. The left figure is the most obvious one, we simply plot the surface energies calculated with the abovementioned equation. As the number of atoms in the configurations changes, one cannot simply compare the energies to each other, and thus drawing a conclusion from the left figure would be somewhat ambiguous. In the right figure, we have plotted the surface energies of the cases where there is Ag in

the slab so that we have subtracted the surface energy of the clean Cu geometry with the corresponding oxygen coverage from them. Thus we can negate the effect of there being different number of atoms in different geometries, and thus we can compare the energetics with each other. Looking at the right figure, we can see that with zero oxygen coverage, it is clearly energetically most favourable for the Ag layer to reside on top of the Cu slab. With even .25 ML of oxygen on the surface, the geometries where the Ag layer resides on the 2nd or the 3rd layer become energetically more favourable, and as the oxygen coverage increases, the difference becomes even clearer. Comparing the curves where the Ag layer resides in either the 2nd or the 3rd layer to each other, we can see that it is energetically more favourable for the Ag layer to reside on the 2nd layer than in the 3rd, that is, right after the oxidized Cu layer. As Hirsimäki *et al.* discovered in their experiment, when Ag/Cu(100) is exposed to O_2, with long enough exposure time the Ag segregates far from the surface. Their measurement devices could penetrate about 10 atomic layers, and there was no Ag or Ag oxides to be detected in that range. Instead they detected Cu oxides, very similarly to the case of clean Cu oxidation.

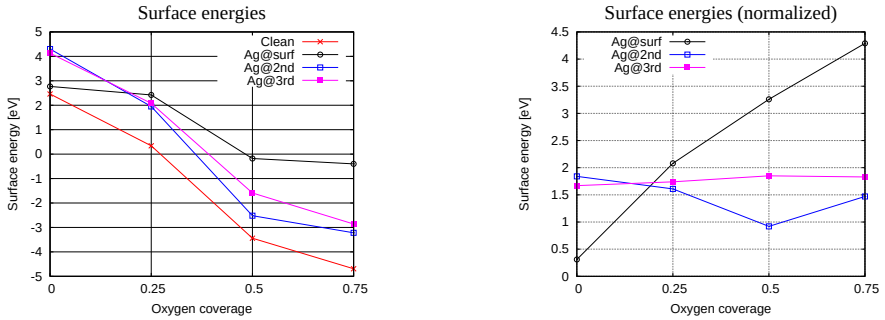

Figure 3.6: Surface energies versus surface O concentration. In the left figure, "Clean" is the case with no silver present. In both figures, Ag@surf, Ag@2nd and Ag@3rd represent the situations where the Ag monolayer is either on top of the Cu slab, in the second layer, or the third, respectively. In the right figure, the energies of the "Clean" case has been subtracted from the Ag cases, thus giving us means to see how the location of the Ag monolayer affects the energetics.

Thus, in the light of our simulations and the results of Hirsimäki *et al.*, one could argue the following: When Ag/Cu oxidizes, Cu atoms segregate from the bulk towards the surface, and form Cu oxides with the adsorped oxygen. A following geometry is then formed: There is a Cu/O phase on the surface, a Cu/Ag alloy under that, and more or less clean Cu in the bulk. Possible reasons for this segregation phenomenon are the size mismatch of Ag and Cu, and the fact that Cu reacts much stronger with oxygen than Ag.

3.2 FeCrNi duplex steels

As mentioned earlier in the Introduction, stainless steels are an important and widely used family of engineering materials, and the main stainless groups are austenitic and ferritic steels [4]. Recently, a third important group is developing around the so called duplex grades [45, 46, 47]. Duplex steels have a peculiar microstructure containing approximately equal amount of ferrite and austenite phases. These steels offer a unique combination of outstanding mechanical performance and appropriate corrosion resistance and present promising alternative materials for various technological applications. Furthermore, since duplex steels usually have twice the mechanical strength of conventional steels, the material cost may significantly be reduced with this class of materials.

Experimental studies, as well as semi-empirical attempts, have been made to describe the phase equilibrium in duplex stainless steels [48, 49, 50, 51, 52]. However, due to the complexity of the problem, little is known about the behaviour and formation of duplex steels at the atomic scale. To remedy this lack, we performed a series of *ab initio* electronic structure and total energy calculations for the austenitic and ferritic steels to study the phase stability as a function of chemical composition. The phenomenon of duplex phase formation is a complex one, and we cannot model everything with our model, so certain approximations are made. We model the two alloy phases with their main building blocks, namely, the austenitic phase is represented with a face centered cubic (fcc) alloy, and the ferrite steel by a body centered cubic (fcc) alloy. Both phases are treated as substitutional random alloys, and short range order and local relaxation effects are omitted.

Industrial grade duplex steels consist of a multitude of atomic species, and it is well known that the alloying species affect the phase balance in duplex steel grades. It is also well known that interstitials, namely C and N, strongly stabilize the austenitic phase. However, in the present study, it is not feasible to model each of the alloying species separately, nor would it be possible to model the interstitials with the chosen method. Also, the major and most important alloying elements for duplex steels are Cr and Ni and the duplex grades are developed around the two elements and the phase constitution determined by them. Therefore, it is very important to understand the ternary Fe-Cr-Ni system in order to understand the duplex grades. Although the study is made with the ternary Fe-Cr-Ni alloy, we can see the gained *ab-initio* understanding in a broader concept: in this study, Ni represents all those alloying elements that stabilize the austenitic phase (Ni, C, N, Mn, etc.) and Cr represents those alloying elements that stabilize the ferrite phase (Cr, Mo, Si, Nb, V, Al, etc.). It should be noted that since Ni and Cr are thermodynamically different from those elements which they represent, they can be seen "equal" to the those

elements only in the sense that they stabilize the same phase. Also, one can not claim that, say, 10% of Ni in this study would have the same effect in stabilizing the austenitic phase as 10% of C; rather, we can say that 10% of Ni has the same effect as *some* amount of C.

At low temperature, the magnetic structure of Fe-Cr-Ni ternary alloys can be antiferromagnetic, spin-glass or ferromagnetic, depending on Ni and Cr content [53]. At room temperature, the austenitic phase is paramagnetic, whereas the ferritic phase is ferromagnetic. Therefore, at room temperature, we can not examine the magnetic free energy of the two phases on an equal footing. Due to that, we limit ourselves in this study to temperatures high enough for the ferritic phase to be beyond its transition temperature, so that the two phases can be compared to each other unbiasedly. We model the paramagnetic ternary $Fe_{1-c-n}Cr_cNi_n$ system by an alloy with randomly distributed chemical species and local magnetic moments, *i.e.* by a four component random $Fe^{\uparrow}_{(1-c-n)/2}Fe^{\downarrow}_{(1-c-n)/2}Cr_cNi_n$ alloy. Here the arrows represent the two magnetic moments oriented up ($\uparrow$) and down ($\downarrow$). This disordered local moment (DLM) approach accurately describes the effect of loss of the net magnetic moment above the transition temperature [54, 55].

We chose the lower limit of the concentration range of Cr to be 12%, given by the stainless requirement[56], and the upper range was chosen to be 32%, as that is near the maximum amount of Cr that is soluble in binary Fr-Cr and Fe-Ni alloys at these temperatures. As all duplex steel alloys contain some elements that fall under the "Ni-equivalent" category, we chose the lower limit of Ni to be 4%, and the upper limit was chosen to be 32%. That much Ni will probably never be seen in commercial duplex grades because of its price, but one must keep in mind that in our calculations, Ni represents all "Ni-equivalents". We performed the calculations for the given range of Cr and Ni compositions, with 4% increments for both alloying species. We calculated the total energies of the (one-atom) system for 7 different values for the lattice parameter. From that data, we deduced, using the Murnaghan equation of state [57], the exact total energy of the system, as well as its equilibrium lattice parameter, and bulk modulus.

From the available data, we can approximate the Gibbs energy of the $Fe_{1-c-n}Cr_cNi_n$ random alloy by

$$G^{str}(c,n) = H^{str}(c,n) - T \cdot \left[S_{conf}(c,n) + S^{str}_{mag}(c,n)\right] + F^{str}_{vib}(c,n), \tag{3.2}$$

where *str* stands for fcc or bcc and T is the temperature. H is the enthalpy, S_{conf} the configurational entropy, S_{mag} the magnetic entropy and F_{vib} the vibrational free energy. The terms $H^{str}(c,n)$ are obtained directly from the self-consistent EMTO calculations. The temperature dependent terms are approximated using the mean-

field expressions. Configurational entropy is given as [58, 59]

$$S_{conf}(c,n) = -k_{\mathrm{B}} \cdot [(1-c-n) \cdot \ln(1-c-n) + c \cdot \ln(c) + n \cdot \ln(n)], \tag{3.3}$$

and magnetic entropy as [60]

$$S^{str}_{mag}(c,n) = -k_{\mathrm{B}} \cdot (1-c-n) \ln\left[1 + \mu^{str}_{\mathrm{Fe}}(c,n)\right], \tag{3.4}$$

where k_{B} is the Boltzmann constant, and $\mu^{str}_{\mathrm{Fe}}(c,n)$ are the local magnetic moments of the Fe atoms. They are obtained from EMTO calculations, and they depend on the crystal structure and chemical composition. We also include an estimate of the vibrational free energy, and we estimate that according to the Debye model, as:

$$F^{str}_{vib}(c,n) = -k_{\mathrm{B}}T \left[\frac{3}{(\Theta_{\mathrm{D}}/T)^3} \int_0^{\Theta_{\mathrm{D}}/T} \frac{x^3}{e^x - 1} dx - 3\ln(1 - e^{-\Theta_{\mathrm{D}}/T}) - \frac{9\Theta_{\mathrm{D}}}{8T} \right], \tag{3.5}$$

where Θ_{D} is the Debye temperature. Note that Θ_{D} depends on the crystal structure, composition and temperature. Within the simplest Debye approximation, the elastic Debye temperature is obtained from the equilibrium atomic radius (Wigner-Seitz radius) w, atomic mass M, Poisson's ratio ν, and bulk modulus B as

$$\Theta_{\mathrm{D}} = \frac{h}{k_{\mathrm{B}}} \left(\frac{4\pi}{3} \right)^{-1/6} F(\nu) \left(\frac{wB}{M} \right)^{1/2}, \tag{3.6}$$

where h is the Planck constant. An explicit expression for the function $F(\nu)$ is given in Ref. [61]. In the present application, the Poisson's ratio was assumed to be 1/3, *i.e.* $F(\nu) = 0.69$. The phase stability of a ternary system is obtained from the common-tangent plane construction [62]. Our final result, the *ab initio* phase stability map, is constructed this way, as well as two other maps which have some of the approximated entropy/energy contributions omitted. The aforementioned maps which have some entropy/energy contributions missing were constructed in order for us to see how the particular entropy/energy contribution affects the phase stability map. These are discussed in detail in Publication IV.

The process of constructing the phase stability map of a ternary alloy is a complex one. Let us, at this point, simplify the two-dimensional problem to a one-dimensional one by assuming the Cr content of the alloy constant ($c = c_0$). We denote the lowest and the highest Ni content by α and β, respectively. Then the Gibbs free energy of formation for the crystal structure *str* is obtained as

$$\Delta G^{str}(c_0,n) = G^{str}(c_0,n) - (1-n) \cdot A - n \cdot B \tag{3.7}$$

where A and B are the two reference energies. As standard states, we take the

fcc phase at high-Ni end and the bcc phase at low-Ni end, with Gibbs energies $G^{\beta} \equiv G^{\mathrm{fcc}}(c_0, \beta)$ and $G^{\alpha} \equiv G^{\mathrm{bcc}}(c_0, \alpha)$, respectively. With this choice, we have

$$\Delta G^{str}(c_0, n) = G^{str}(c_0, n) - [(\alpha - n) \cdot G^{\beta} - (\beta - n) \cdot G^{\alpha}]/(\alpha - \beta). \tag{3.8}$$

We have plotted the Gibbs free energies, as well as the components of which it consists, in Fig. 3.7, for both structures. The added terms are temperature dependent, and they are plotted at the temperature of $T = 1000$K. One can clearly see that if we did not include any of the approximated entropy/energy terms, regarding only the mixing enthalpy, there would be no duplex phase present at all. We can thus deduce that the entropy contributions play a very important role in the formation of the duplex region. This conclusion is also evident when comparing the phase stability maps with varying levels of entropy contributions included to each other.

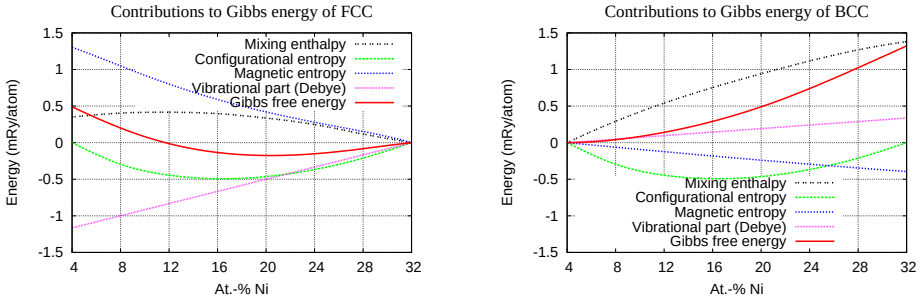

Figure 3.7: The contributing energy and entropy terms that are summed up to form Gibbs free energy (black curve in the figures). These curves are plotted as a function of Ni content, and Cr content is fixed to 16%.

Now, we can determine from the Gibbs free energies which structure is energetically the most favourable at a certain concentration. The Gibbs energy curves from Fig. 3.7 are compared to each other in Fig. 3.8. By drawing a common tangent to the fcc and bcc Gibbs energies, we find the concentration interval ($2 - 19\%$ Ni), where the segregated system (duplex) is energetically more favorable than either one of the single-phase alloys. Within this two-phase field region, the system breaks in thermodynamic equilibrium into Ni-enriched fcc and Ni-depleted bcc components. To the left of the duplex region the bcc phase is stable, and to the right, the fcc is stable.

As mentioned above, we discussed the quasi-binary alloy where we have fixed the Cr content for the sake of example only. In the case of ternary alloys, the problem is two-dimentional, and thus a graphic representation of how the phase stability map is obtained is harder to give compared to the one-dimensional case, but the method is rather similar, and easy enough to understand in light of the one-dimensional case. Instead of plotting a tangent line to two curves, imagine a tangent plane plotted so that it touches two concave surfaces.

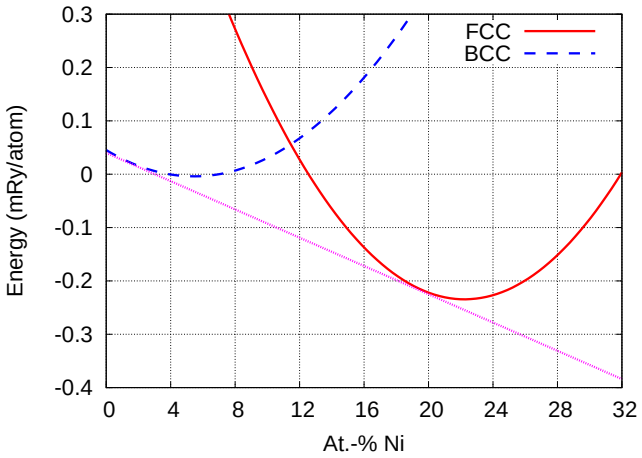

Figure 3.8: Gibbs free energies for bcc and fcc $Fe_{0.84-n}Cr_{0.16}Ni_n$ plotted as a function of Ni content. The duplex region corresponds to Ni concentration range between the points where the Gibbs energies touch their common tangent.

In Fig. 3.9 we show the theoretical phase stability map derived with the above described common-tangent plane construction (topmost figure). The bottom left figure, given as comparison, is a schematic of the Schäffler phase diagram for stainless steels [4]. The diagram describes the empirically determined weld micro structures, and corresponds to the situation around 1300K. In this figure, "The Ni-equivalents" represents a number of different atomic species, as do the "Cr-equivalents" (see the figure caption).

As another reference, shown in Fig. 3.9 at the bottom right, we use the phase diagram obtained at 1123 K for the Fe-Cr-Ni systems using thermodynamic assessment [48] based on subregular solution model [63, 64]. Knowing that it reproduces very well the experimental phase boundaries by Eriksson [48, 65], we can consider it as accurate as experimental data.

Taking into account the approximations made in our study, the agreement between the present theoretical phase diagram and the reference diagrams is fairly good. We have thus established *ab initio* a description to this complex problem, although notable approximations were made. We can also conclude that the entropy contributions, along with the vibrational free energy, constitute an important factor on defining the stability fields of different phases.

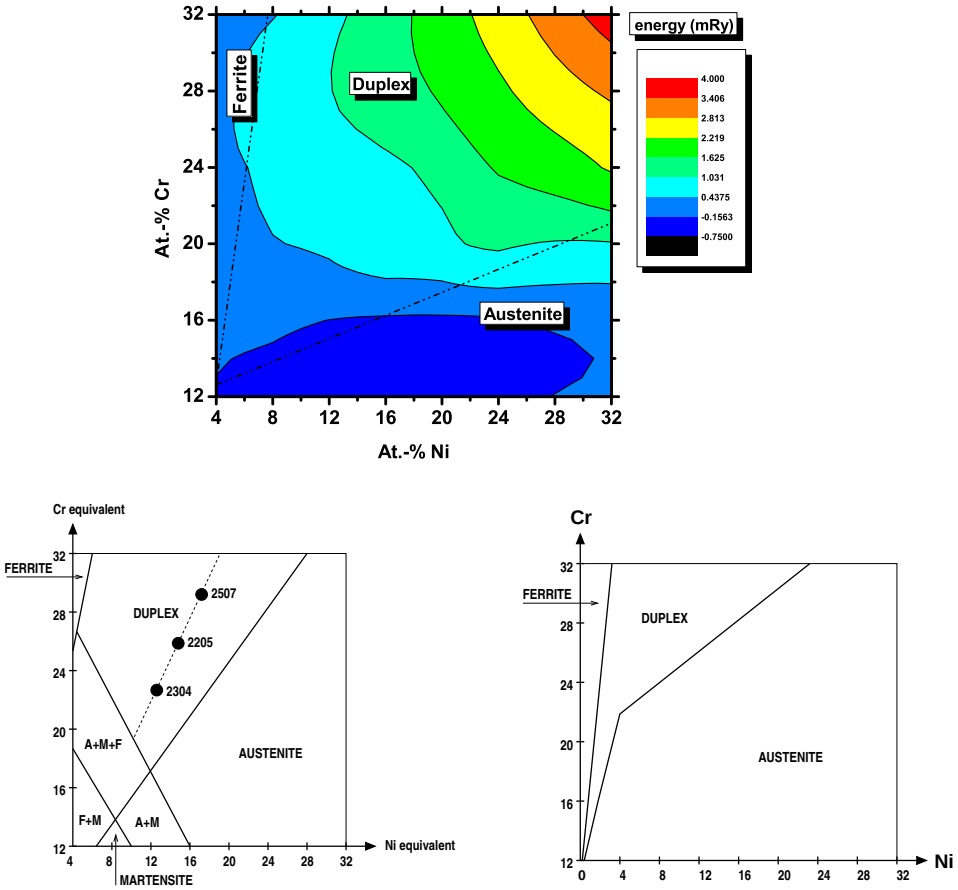

Figure 3.9: Top: Theoretical high-temperature phase diagram for paramagnetic $Fe_{1-c-n}Cr_cNi_n$. The two dashed lines mark the estimated ferrite-duplex and duplex-austenite boundaries. The colors indicate the Gibbs free energy at a certain point. Shown are $\Delta G_1^{\mathrm{bcc}}(c,n)$ for those concentrations where $\Delta G_1^{\mathrm{bcc}} < \Delta G_1^{\mathrm{fcc}}$, and $\Delta G_1^{\mathrm{fcc}}(c,n)$ for those concentrations where $\Delta G_1^{\mathrm{fcc}} < \Delta G_1^{\mathrm{bcc}}$. Bottom left: Schematic of the Schäffler phase diagram. Concentrations are given in weight percent. The numbers represent a few commercially available duplex steel alloys. The horizontal axis, "Ni-equivalent", represents atomic species Ni, C, N, Mn, etc. (austenitic stabilizers). The vertical axis, "Cr-equivalent", represents atomic species Cr, Mo, Si, Nb, V, Al, etc. (ferrite stabilizers). Bottom right: Schematic of the semi-empirical phase diagram obtaiden by Hertzman *et al* using thermodynamic assesment.

Chapter 4

Concluding remarks

In the previous chapter, the results gained through the simulations were presented and discussed. It must be kept in mind that the reality of the discussed topics is a complex one, and a simulation model is never an exact representation of reality, but a construct collected together from the theoretical understanding. However, both cases are known to agree with experiments: VASP, the simulation code used for the Ag/Cu simulations, is a widely used code and thus tested under a myriad of conditions, and the agreement between our EMTO results and experiments was notably good. In situations like this, the simulated result is far from guesswork: we know that the result is correct by comparing it to experiments, but there is much one can see in simulations that is not visible in experiments. Time scales several orders of magnitude shorter can be monitored, and the electronic state of the system is fully known at each point in space, and time.

The oxidation process of clean Cu(100) surface, with no alloying elements whatsoever, is not yet known. The process takes many phases, which should be investigated in varying time and length scales, and that would require the use of several methods. After initial oxidation (adsorption of O to the surface) the forming oxide patches start to grow in a peculiar fashion: elongated islands that are oriented parallel or perpendicular to each other, start to form [66]. After that a deeper oxide layer is formed. This information is observable via experiments, but adequate theoretical explanations, linking the atomistic details and the observed macroscopic features, do not exist, yet. So, when we add to a field with that many unknowns an additional phenomenon, namely, the effect of admetals, it gets even more complex.

Therefore, to explain the dynamics of such a case which is an interplay of several contributing phenomena, understanding of the whole situation must be gathered in parts, and in a step-by-step manner. When a part of the problem is understood, the number of unknowns is reduced, and future research can focus on another aspect. The additional understanding provided by our studies can be seen to pace

the collective scientific understanding one step further. What we have clearly established is this: the presence of Ag on a Cu(100) surface, even in such small quantities as 11%, clearly inhibits chemisorption of O_2. We see in the MD simulations, that the O_2 molecule can steer sideways to a four-fold hollow site, and physisorb there. If there were a complete Ag overlayer, what would the adsorption dynamics be then? To answer that, one would have to run a similar simulation, but with a much larger supercell (because of the c(2×10) reconstruction). Since both the exposure study and the MBSS study indicate that the adsorption of O_2 happens even with a monolayer of Ag, it would be interesting to know how many monolayers one needs to prevent it, if there is such a limit. As for the oxygen induced reconstruction, we showcased an *ab initio* proof that the systems where Ag segregates downwards, away from the surface, are indeed favoured to systems where Ag is on top of the surface, near the O atoms. What kind of structure is formed when Ag/Cu oxidizes, and how, is a question that was out of the scope of our studies, and still needs an answer.

In the other half of this study, we studied the phase stability of paramagnetic duplex steel alloys. We limited ourselves in high temperatures to be able to treat the entropies from an equal footing. Moreover, we used rather general approximations to represent the additional entropy and free energy contributions present. We also omitted all long-range effects, and the effect of grain boundaries. Still, this is a rather novel study, because this kind of study has not yet been made (to our knowledge), and our results agree reasonably well with experiments. To extend this study further, we are conducting a study about the mechanican strength of duplex steels by calculating surface energies of non-segregated FeCrNi surfaces. After that, one could calculate surface segregation profiles, which, in turn, would make it possible for one to perform simulations on how certain chemical reactions occur on the surface. This would be quite a significant addition to the *ab initio* understanding of duplex steels, but that would obviously take much work to achieve.

A lot of nature's mysteries are still unraveled, and it seems that computational physics has much to give in the future also. After all, all simulation codes are based on theoretical knowledge of their time, and as time progresses, more experiments are made and more eloquent theories developed, and thus more accurate simulation models are constructed. Also, as the computational power of (super)computers increases, more and more complicated simulations can be executed. In this light, computational physics represents a notable part of the cutting edge of science.

In conclusion, I would like to borrow a beautiful metaphor from Esko Valtaoja: Even if a single scientist or a group can only achieve so much, by their efforts, they all contribute to the collective pool of scientific understanding, thus adding their share, like a grain of sand to the temple of science.

Bibliography

[1] Émile Durkheim: The Elementary Forms of Religious Life, The Free Press, New York, (1965).

[2] A. Christensen, A. V. Ruban, P. Stolze, K. W. Jacobsen, H. L. Skiver, and J. K. Nørskov: Phase diagrams for surface alloys, Phys. Rev. B, **56**, 5822-5834, (1997).

[3] H. Over, Y. D. Kim, A. P. Seitsonen, S. Wendt, E. Lundgren, M. Schmidt, P. Varga, A. Morgante, and G. Ertl: Atomic-Scale Structure and Catalytic Reactivity of the RuO_2(110) Surface, Science, **287**, (2000).

[4] J. Charles: Past, present and future of the duplex stainless steels. Arcelor Mittal Stainless, (2007).

[5] G. Kresse and J. Hafner: Norm-conserving and ultrasoft pseudopotentials for first-row and transition elements, J. Phys. Cond. Mat., **6**, 8245, (1994).

[6] G. Kresse and J. Furthmüller: Efficiency of ab-initio total energy calculations for metals and semiconductors using a plane-wave basis set, Comput. Mat. Sci. **6**, 15, (1996).

[7] G. Kresse and J. Furthmüller: Efficient iterative schemes for *ab initio* total energy calculations using a plane-wave basis set, Phys. Rev. B, **54**, 11169, (1996).

[8] G. Kresse and J. Joubert: From ultrasoft pseudopotentials to the projector augmented-wave method, Phys. Rev. B, **59**, 1758, (1999).

[9] D. Vanderbilt: Soft self-consistent pseudopotentials in a generalized eigenvalue formalism, Phys. Rev. B, **41**, 7892-7895, (1990).

[10] O. K. Andersen, O. Jepsen, and G. Krier: Exact Muffin Tin Orbital Theory, World Scientific Publishing Co., Singapore, (1994).

[11] L. Vitos, I. A. Abrikosov, and B. Johansson: Anisotropic lattice distortions in random alloys from first-principles theory, Phys. Rev. Lett. **87**, 156401-1, (2001).

[12] L. Vitos: Total-energy method based on the exact muffin-tin orbitals theory, Phys. Rev. B, **64**, 014107, (2001).

[13] P. Soven, Phys. Rev. **156**, 809, (1967).

[14] D. W. Taylor: Vibrational Properties of Imperfect Crystals with Large Defect Concentrations, Phys. Rev. **156**, 1017 (1967).

[15] M. Born and J. R. Oppenheimer: Zur quantentheorie der molekaln, Ann. Physik., **84**, 457, (1927).

[16] N. W. Ashcroft and N. D. Mermin: Solid state physics, Thomson Learning, London, (1976).

[17] C. Møller and M. S. Plesset: Note on an Approximation Treatment for Many-Electron Systems, Phys. Rev., **46**, 618–622, (1934).

[18] J. W. S. Rayleigh: Theory of Sound, 2nd edition, vol. 1, p. 115-118, Macmillan, London (1894).

[19] E. Schrödinger: Quantisierung als Eigenwertproblem, Ann. Phys., **79**, 361-76, (1926).

[20] P. Hohenberg and W. Kohn: Inhomogenous electron gas, Phys. Rev., **136**, B864, (1964).

[21] N. D. Mermin: Thermal properties of the inhomogeneous electron gas, Phys. Rev., **137**, A1441-1443, (1965).

[22] W. Kohn and L. Sham: Self-consistent equasions including exchange and correalation effects, Phys. Rev., **140**, A1133, (1965).

[23] D. C. Langreth and J. P. Perdew: Theory of nonuniform electronic systems. I. Analysis of the gradient approximation and a generalization that works, Phys. Rev. B, **21**, 5469-5493, (1980).

[24] D. C. Langreth and M. J. Mehl: Beyond the local-density approximation in calculations of ground-state electronic properties, Phys. Rev. B, **28**, 1809-1834, (1983).

[25] J. P. Perdew and Y. Wang: Accurate and simple density functional for the electronic exchange energy: Generalized gradient approximation, Phys. Rev. B, **33**, 800-8802, (1986).

[26] J. P. Perdew: Density-functional approximation for the correlation energy of the inhomogeneous electron gas, Phys. Rev. B, **33**, 8822-8824, (1986).

[27] A. Groß: Theoretical Surface Science A Microscopic Perspective, Berlin, Springer, (2003).

[28] Richard M. Martin: Electronic Structure, Basic Theory and Practical Methods, Cambridge university press, (2004).

[29] S. Clark: Complex Structure in Tetrahedral Semiconductors (1996), *http://cmt.dur.ac.uk/sjc/thesis/thesis/node14.html*, [retrieved 2010-09-09].

[30] H. J. Monkhorst and J. D. Pack: Special points for Brillouin-zone integrations, Phys. Rev. B, **13**, 5192, (1977).

[31] M. D. Segall: An ab Initio Study of Biological Systems, Clare Hall, Cambridge, (1997), *http://www.tcm.phy.cam.ac.uk/ mds21/thesis/thesis.html*, [retrieved 2010-10-11].

[32] D. R. Hamann, M. Schlüter, and C. Chiang: Norm-Conserving pseudopotentials, Phys. Rev. Lett., **43**, 1494, (1979).

[33] G. B. Bachelet, D. R. Hamann, and M. Schlüter: Pseudopotentials that work: From H to Pu, Phys. Rev. B, **26**, 4199, (1982).

[34] N. Troullier and J. L. Martins: Efficient pseudopotentials for plane-wave calculations, Phys. Rev. B, **43**, 1993 (1991).

[35] P. E. Blöchl: Projector augmented-wave method, Phys. Rev. B, **50**, 17953, (1994).

[36] R. Car and M. Parrinello: Unified Approach for Molecular Dynamics and Density-Functional Theory, Phys. Rev. Lett., **55**, 2471, (1985).

[37] O. K. Andersen, T. Saha-Dasgupta, R. W. Tank, C. Arcangeli, O. Jepsen, and G. Krier: Developing the MTO Formalism, Max-Planck-Institut, (1999).

[38] Levente Vitos: Computational Quantum Mechanics for Materials Engineers, Springer, (2007).

[39] D. D. Johnson, D. M. Nicholson, F. J. Pinski, B. J. Gyorffy, and G. M. Stocks: Density-Functional Theory for Random Alloys: Total Energy within the Coherent Potantial Approximation, Phys. Rev. Let. **56**, 2088-2091, (1986).

[40] S. Faulkner and G. M. Stocks: Theory of the specific-heat coefficient of a Hume-Rothery alloy, Phys. Rev. B **23**, 5628, (1981).

[41] J. Hayoz, D. Naumovic, R. Fasel, P. Aebi, and L. Schlapback: Growth of Ag on Cu(001) studied by full-hemispherical X-ray photoelectron diffraction, Surf. Sci. **373**, 153, (1997).

[42] M. Hirsimäki, M. Lampimäki, K. Lahtonen, I. Chorkendorff, and M. Valden: Investigation of the role of oxygen induced segregation of Cu during Cu_2O formation on Cu{100}, Ag/Cu{100} and Cu(Ag) alloy, Surf. Sci., **583**, 157-165, (2005).

[43] P. Junell, M. Ahonen, M. Hirsimäki, and M. Valden: Influence of surface modification on the adsorption dynamics of O_2 on Cu100, Surf. Rev. and Lett., **11**, 457-461, (2004).

[44] P. T. Sprunger, E. Lægsgaard, and F. Besenbacher: Growth of Ag on Cu(100) studied by STM: From surface alloying to Ag superstructures, Phys. Rev. B, **54**, 8163, (1996).

[45] F. H. Hayes: Phase equilibria in duplex stainless steels, J. Less. Common Met., **114**, 89-96, (1985).

[46] R. M. Redmond and J. D. Redmond: Practical guide to using duplex stainless-steels, Mater. Perform., **29**, 57-62, (1990).

[47] F. H. Hayes, M. G. Hertingtom, and R. D. Longbottom: Thermodynamics of duplex stainless-steels, Mater. Sci. Tech., **6**, 263-272, (1990).

[48] S. Hertzman and Bo Sundman: A thermodynamic analysis of the Fe-Cr-Ni system, Scand. J. Metallurgy, **14**, 94-102, (1985).

[49] S. Hertzman, P. J. Ferreira, and B. Brolund: An experimental and theoretical study of heat-affected zone austenite reformation in three duplex stainless steels, Metall. Trans. A, **28**, 277, (1997).

[50] S. Atamert and J. E. King, The Third International Conference on Duplex Stainless Steels, ed. by J. Charles and S. Bernhardsson: Beaune, France: Les Editions de Physique, 701-710, (1991).

[51] R. Mundt and H. Hoffmeister, in Stainless Steel 84, The Institute of Metals, London, 315, (1984).

[52] K. Ameyama, G. C. Weatherly, and K. C Aust, Acta Metall. Mater. **40**, 1835 (1992).

[53] A. K. Majumdar and P. v. Blanckenhagen: Magnetic phase diagram of $Fe_{80-x}Ni_xCr_20$ ($10 \leq x \leq 30$) alloys, Phys. Rev. B, **29**, 4079-4085, (1984).

[54] B. L. Györffy, A. J. Pindor, J. Staunton, G. M. Stocks, and H. Winter: A first-principles theory of ferromagnetic phase transitions in metals, J. Phys. F, **15**, 1337, (1985).

[55] J. Staunton, B. L. Györffy, A. J. Pindor, G. M. Stocks, and H. Winter: The disordered local moment picture of itinerant magnetism at finite temperatures, J. Magn. Magn. Mater. **45**, 15, (1984).

[56] G. Wrangler: An htroduction to Corrosion and Protection of Metals: Chapman and Hall, (1985).

[57] F.D. Murnaghan: The Compressibility of Media under Extreme Pressures, Proc. Natl. Acad. Sci., **30**, 244-247, (1944).

[58] M. Ropo: *Ab initio* study of the geometric depencence of AgPd surface segregation, Phys. Rev. B, **74**, 195401, (2006).

[59] M. Ropo, K. Kokko, L. Vitos, and J. Kollár: Segregation at the PdAg(111) surface: Electronic structure calculations, Phys. Rev. B, **71**, 045411, (2005).

[60] L. Vitos, P. A. Korzhavyj, and B. Johansson: Evidence of large magnetostructural effects in austeinitic stainless steels, Phys. Rev. Lett., **96**, 117210, (2006).

[61] P. Söderlind, L. Nordström, L. Yongming, and B. Johansson: Relativistic effects on the thermal expansion of the actinide elements, Phys. Rev. B, **42**, 4544, (1990).

[62] M. Hillert: Phase Equilibria, Phase Diagrams and Phase Transformations, Cambridge University Press, Cambridge, (2008).

[63] B. Sundman and J. Agren: A regular solution model for phases with several components and sublattices, suitable for computer applications, J. Phys. Chem. Sol. **42**, 297, (1981).

[64] M. Hillert and L.-I. Staffansson: The regular solution model for stoichiometric phases and ionic melts, Acta Chem. Scan., **24**, 3618, (1970).

[65] T. Eriksson, Thesis, Royal Inst. of Techn., Stockholm (1962).

[66] G. Zhou and J. C. Yang: Formation of Quasi-One-Dimensional Cu_2O Structures by *in situ* Oxidation of Cu(100), Phys. Rev. Lett. **89**, 106101, (2002).

[67] P. Fornasiero, T. Montini, M. Graziani, S. Zilio, and M. Succi: Development of functionalized Fe-Al-Cr alloy fibres as innovative catalytic oxidation devices, Catal. today, **137**, 475-482, (2008).